INTERFACE

royalsocietypublishing.org/journal/rsif

Review

Cite this article: Arzani A, Dawson STM. 2021 Data-driven cardiovascular flow modelling: examples and opportunities. *J. R. Soc. Interface* **18**: 20200802.
https://doi.org/10.1098/rsif.2020.0802

Received: 5 October 2020
Accepted: 18 January 2021

Subject Category:
Life Sciences–Engineering interface

Subject Areas:
bioengineering, biomedical engineering, biomechanics

Keywords:
blood flow, haemodynamics, data science, sparse sensing, data-driven dynamical systems, reduced-order modelling

Author for correspondence:
Amirhossein Arzani
e-mail: amir.arzani@nau.edu

Data-driven cardiovascular flow modelling: examples and opportunities

Amirhossein Arzani[1] and Scott T. M. Dawson[2]

[1]Department of Mechanical Engineering, Northern Arizona University, Flagstaff, AZ, USA
[2]Department of Mechanical, Materials and Aerospace Engineering, Illinois Institute of Technology, Chicago, IL, USA

AA, 0000-0002-3706-7909

High-fidelity blood flow modelling is crucial for enhancing our understanding of cardiovascular disease. Despite significant advances in computational and experimental characterization of blood flow, the knowledge that we can acquire from such investigations remains limited by the presence of uncertainty in parameters, low resolution, and measurement noise. Additionally, extracting useful information from these datasets is challenging. Data-driven modelling techniques have the potential to overcome these challenges and transform cardiovascular flow modelling. Here, we review several data-driven modelling techniques, highlight the common ideas and principles that emerge across numerous such techniques, and provide illustrative examples of how they could be used in the context of cardiovascular fluid mechanics. In particular, we discuss principal component analysis (PCA), robust PCA, compressed sensing, the Kalman filter for data assimilation, low-rank data recovery, and several additional methods for reduced-order modelling of cardiovascular flows, including the dynamic mode decomposition and the sparse identification of nonlinear dynamics. All techniques are presented in the context of cardiovascular flows with simple examples. These data-driven modelling techniques have the potential to transform computational and experimental cardiovascular research, and we discuss challenges and opportunities in applying these techniques in the field, looking ultimately towards data-driven patient-specific blood flow modelling.

1. Introduction

We live in the age of data science, where the wealth of data and advances in data processing and computational power are beginning to affect every field. The field of cardiovascular fluid mechanics is no exception. Blood flow modelling has come a long way from Womersley's analytical Navier–Stokes solution for incompressible pulsatile flow in tubes during the 1950s [1] to the recent Food and Drug Administration approval of patient-specific computational fluid dynamics (CFD) estimation of pressure drop in coronary artery disease [2]. Advances in computational and experimental characterization of blood flow along with promising advances in the field of data science provide a unique opportunity for exciting developments in the field of cardiovascular fluid mechanics with the potential to transform our understanding of cardiovascular disease.

In modelling cardiovascular disease, blood flow and haemodynamics data are provided by multiple modalities. Patient-specific CFD, *in vivo* four-dimensional (4D) flow magnetic resonance imaging (MRI), and *in vitro* particle image velocimetry (PIV) or particle tracking velocimetry are leading modalities in providing three-dimensional time-resolved blood flow data. However, none of these modalities are perfect. Numerical error, parameter uncertainty, imaging artefacts, low spatio-temporal resolution, and measurement noise are among the limitations of these methods. Some open questions are summarized: How can we improve the quality and accuracy of the data generated by either of these modalities? If we possess data from more than one modality, is it possible

THE ROYAL SOCIETY PUBLISHING

to generate new data with superior accuracy with respect to either dataset? How can we best extract useful information from these datasets? Given the complex spatio-temporal patterns in haemodynamics, is it possible to derive simplified representations of the data that facilitate physical understanding and further modelling? Data-driven modelling techniques provide potential means to answer these questions.

This work will focus on data-driven modelling techniques that seek to exploit underlying low-dimensionality and sparsity in data, and in the systems that generate such data. These methods combine classical data-driven analysis techniques originating from principal component analysis (PCA) developed over a century ago by Pearson [3], with more recent advances in data-driven dynamical systems analysis [4–7], compressive sensing [8–10], and optimal data reconstruction and interpolation [11–13]. In the class of methods that we focus on, we are typically interested in representing complex high-dimensional data in a simpler low-dimensional space, while also potentially dealing with corrupted or under-resolved data. Note that the class of data-driven modelling methods considered here share some similarities and distinctions with classical machine learning and deep learning applications. In both techniques, we are interested in learning patterns in data. In deep learning with neural networks, we are seeking optimized function approximators that are capable of revealing hidden patterns in data. Similarly, in the data-driven modelling methods discussed here, we are often interested in finding optimized models that can represent the data. A major distinction is that in what we present as data-driven modelling, we often deal with small and sometimes corrupted datasets, whereas classical deep learning techniques typically require very large datasets. Additionally, lack of interpretability is a shortcoming of current deep learning techniques, which is an important issue in fluid mechanics where we are often interested in the flow physics [14]. On the other hand, data-driven reduced-order modelling facilitates physical interpretation [15].

The fact that high-dimensional datasets are (at least approximately) low rank can be observed empirically across a broad range of applications, and this ubiquitous phenomenon can also be demonstrated theoretically under certain assumptions [16]. By definition, a low-rank dataset can be represented by a small number of functions. For example, low-rank data representing a snapshot in time of the state of a system can be expressed as a certain linear combination of such functions, for any time. These functions can be viewed as a small number of elements of a basis that spans the space of all possible data, whether physically realistic or not. The fact that any physically realistic snapshot can be represented by a small number of basis functions means that a dataset consisting of many such snapshots is sparse in this basis. The existence of a basis in which the data are sparse allows for the application of several related techniques that exploit this sparsity, such as reconstruction of full-state information from a limited number of sensor measurements, which may be placed randomly, or more optimally if given more information about the system. Also, by considering data generated from a given physical system as having some type of sparsity in an appropriate basis, we can further consider notions of sparsity in the underlying equations that can generate or approximate the data. For example, if approximating a given physical system by a set of nonlinear ordinary differential equations involving a small number of state variables, the structure of the equations might typically only require a small number of non-zero terms. These non-zero terms are sparse in the space of all possible terms and can be identified from data using sparsity-promoting identification methods [7].

In this paper, we review several data-driven modelling techniques and provide examples of how they could be used in cardiovascular fluid mechanics research. The overarching goal of these techniques is to facilitate data interpretation, augment data when the data are incomplete or low-resolution, improve the quality of data, and leverage data from multiple modalities to improve data fidelity. Many of these techniques are based on a well-established, yet diverse set of mathematical tools. Familiarity with these fundamental mathematical techniques and concepts may enable cardiovascular researchers to come up with customized techniques to improve their models. The objective of this paper is to provide an introduction to some of these techniques with tangible examples for the cardiovascular fluid mechanics community. To help researchers who would like a more in-depth introduction to these topics, in table 1, we provide a list of excellent books that we recommend for each topic. The list is classified based on several important fundamental and applied mathematical topics that are generally important in data science and data-driven modelling for engineering and applied sciences.

1.1. Paper organization

In each section, we present an important data-driven modelling technique. Each section is divided into subsections where we present the motivation behind the need for the technique, the mathematical theory, example(s) relevant to cardiovascular flow problems, and a short discussion on opportunities for cardiovascular researchers as well as challenges in applying the technique to practical problems. Finally, we briefly discuss a few recent trends in computational mechanics related to data science that could be valuable in cardiovascular biomechanics modelling.

2. Principal component analysis: detecting redundancy and low-dimensionality in data

2.1. Motivation

Thanks to high-performance computing, numerical simulations can provide spatio-temporally highly resolved haemodynamics data. However, often haemodynamics data possess hidden low-dimensionality, which once exposed, can reduce the dimensionality of the data and provide opportunities for advanced data analysis as discussed in the next sections. This is due to the high correlation among temporal snapshots in data (or equivalently, between different locations in space). That is, under an appropriate coordinate system, we can reduce the size of haemodynamics data with minimal loss in accuracy. PCA is based on singular value decomposition (SVD), which is one of the most ubiquitous and powerful matrix transformations in linear algebra [36]. As an aside, note however that PCA (and the independently developed Hotelling analysis [37]) predated much of the theory and numerical analysis of SVD. PCA provides an optimal basis where with the minimum number of independent/uncorrelated modes one may represent the data. In other words, we

Table 1. List of recommended books for an in-depth introduction to fundamental and applied mathematical topics that form the basis of data-driven modelling.

book title	author	comments	ref.
linear algebra			
linear algebra and learning from data	G. Strang	an excellent introduction with emphasis on data-driven modelling. Author's linear algebra video lectures are available on MIT OCW website	[17]
introduction to applied linear algebra: vectors, matrices and least-squares	S. Boyd & L. Vandenberghe	basic linear algebra concepts. S. Boyd's 'Introduction to Linear Dynamical Systems' video lectures covering similar topics are available on Youtube	[18]
numerical linear algebra	L. Trefethen & D. Bau	a standard introductory textbook for numerical implementation of linear algebra algorithms	[19]
statistics			
practical statistics for data scientists: 50+ essential concepts using R and Python	P. Bruce *et al.*	an easy read for essential statistical tools in data-driven modelling	[20]
probability and mathematical statistics: theory, applications, and practice in R	M. Meyer	a comprehensive mathematical introduction to statistical theories	[21]
optimization			
convex optimization	S. Boyd & L. Vandenberghe	the standard textbook for convex optimization. S. Boyd's video lectures based on this topic are available on Youtube	[22]
dynamical systems			
differential equations and dynamical systems	L. Perko	one of the best mathematical introductions to dynamical systems	[23]
nonlinear dynamics and chaos: with applications to physics, biology, chemistry and engineering	S. Strogatz	a simple conceptual and practical introduction to dynamical systems. Strogatz's video lectures based on this topic are available on Youtube	[24]
data assimilation			
data assimilation: methods, algorithms and applications	M. Asch *et al.*	a rigorous and comprehensive introduction to the topic	[25]
data assimilation: a mathematical introduction	K. Law *et al.*	a mathematical introduction with Matlab codes	[26]
compressed sensing (CS) and sparsity			
CS for engineers	A. Majumdar	an excellent practical introduction to CS with different examples such as medical imaging	[27]
sparse modelling: theory, algorithms and applications	I. Rish & G. Grabarnik	a mathematically more detailed introduction to CS and sparsity	[28]
machine learning			
the hundred-page machine learning book	A. Burkov	a concise but informative and conceptual introduction to machine learning	[29]
an introduction to statistical learning	G. James *et al.*	one of the most popular and accessible references in machine learning	[30]
matrix methods in data mining and pattern recognition	L. Eldén	a mathematical introduction to machine learning with emphasis on linear algebra	[31]
reduced-order and data-driven modelling			
reduced basis methods for partial differential equations: an introduction	A. Quarteroni *et al.*	a detailed mathematical introduction to reduced-order modelling of partial differential equations and proper orthogonal decomposition (POD)	[32]

(*Continued*.)

Table 1. (*Continued.*)

book title	author	comments	ref.
turbulence, coherent structures, dynamical systems and symmetry	P. Holmes *et al.*	an introduction to POD with focus on applications in fluid mechanics and turbulence	[5]
dynamic mode decomposition (DMD): data-driven modelling of complex systems	N. Kutz *et al.*	an introduction to reduced-order modelling of dynamical systems using DMD	[33]
data-driven modelling and scientific computation: methods for complex systems and big data	N. Kutz	a comprehensive introductory book on a wide range of data-driven modelling tools and necessary mathematical preliminaries. Kutz's video lectures based on this topic are available on Youtube	[34]
data-driven science and engineering: machine learning, dynamical systems and control	S. Brunton & N. Kutz	an excellent overview of various data-driven modelling techniques. Brunton's video lectures based on this topic are available on Youtube	[35]

seek to find a basis where the data have minimal correlation, and therefore reduced redundancy. What we introduce as PCA in §2.2 is essentially equivalent to what is known as the proper orthogonal decomposition (POD) in fluid mechanics [38], which will be discussed explicitly in §6.2.

2.2. Model theory and background

In PCA, the data are stacked into a rectangular matrix. Here, we arrange the spatial data in n rows and the temporal data in m columns. Therefore, spatio-temporal haemodynamics data for a variable (e.g. velocity) could be arranged into a matrix $\mathbf{X}$

$$\mathbf{X}_{(n\times m)} = [\,\mathbf{W}_1 \quad \mathbf{W}_2 \quad \cdots \quad \mathbf{W}_m\,], \tag{2.1}$$

where the spatial data in each snapshot (time-step) is arranged as a column. This form of data representation will frequently be used throughout the paper. Here, for clarity, we on occasion use subscripts such as $(n \times m)$ to indicate the dimensions of a matrix. The temporal mean of the data at each spatial location is subtracted from each row to define a new matrix $\tilde{\mathbf{X}}$

$$\tilde{\mathbf{X}}_{(n\times m)} = \sqrt{\frac{1}{m}}\left(\mathbf{X}_{(n\times m)} - \bar{\mathbf{x}}_{(n\times 1)}\mathbf{J}_{(1\times m)}\right), \tag{2.2}$$

where $\mathbf{J}_{(1\times m)} = [1\,1\cdots 1]$, and $\bar{\mathbf{x}}_{(n\times 1)} = (1/m)\sum_{j=1}^{m}\mathbf{X}_{ij}$ is a column vector containing the mean of each row. Subsequently, SVD is performed on the processed data matrix

$$\tilde{\mathbf{X}} = \mathbf{U}\mathbf{\Sigma}\mathbf{V}^*, \tag{2.3}$$

where the columns of $\mathbf{U}$ and $\mathbf{V}$ are the left and right singular vectors (which are orthonormal), the diagonal values of $\mathbf{\Sigma}$ are the singular values, and * specifies the complex conjugate transpose. For the 'full' SVD, $\mathbf{U}$ and $\mathbf{V}$ are square matrices, but here we will only need to consider the columns corresponding to nonzero singular values.

The left and right singular vectors are also eigenvectors of the equivalent space- and time-correlation matrices, satisfying

$$\tilde{\mathbf{X}}\tilde{\mathbf{X}}^*\mathbf{u}_j = \sigma_j^2\mathbf{u}_j \tag{2.4}$$

and

$$\tilde{\mathbf{X}}^*\tilde{\mathbf{X}}\mathbf{v}_j = \sigma_j^2\mathbf{v}_j, \tag{2.5}$$

where $\mathbf{u}_j$ and $\mathbf{v}_j$ are the jth columns of $\mathbf{U}$ and $\mathbf{V}$, and σ_j is the jth diagonal entry of $\mathbf{\Sigma}$.

The SVD is unique (up to rotation of the singular vectors in the complex plane), and allows for an 'optimal' low-rank approximation of the original data. More precisely, the rank-r approximation $\tilde{\mathbf{X}}_r$ that minimizes the reconstruction error (using the Frobenius norm)

$$\epsilon_r = \|\tilde{\mathbf{X}} - \tilde{\mathbf{X}}_r\|_F \tag{2.6}$$

is given by

$$\tilde{\mathbf{X}}_r = \mathbf{U}_r\mathbf{\Sigma}_r\mathbf{V}_r^*, \tag{2.7}$$

where $\mathbf{U}_r$ and $\mathbf{V}_r$ contain the first r columns of $\mathbf{U}$ and $\mathbf{V}$, and $\mathbf{\Sigma}_r$ contains the first r rows and columns of $\mathbf{\Sigma}$.

Physically, with the data arranged as described in equation (2.1), the columns of $\mathbf{U}$ denote an ordered set of spatial functions, or 'modes', which represent the principal components of the data. The extent to which a given such function characterizes the data is given by the associated singular value (i.e. the corresponding diagonal entry of $\mathbf{\Sigma}$). The columns of $\mathbf{V}$ (or equivalently, rows of $\mathbf{V}^*$) give information about the relative amplitude of the corresponding spatial mode for each snapshot of data. Time-resolved data are not required to compute the spatial PCA modes, but in the case where time-resolved data are available, these columns of $\mathbf{V}$ are functions of time. Therefore, we can equivalently express equation (2.3) as

$$\tilde{\mathbf{X}} = \sum_{j=1}^{\min(n,m)}\mathbf{u}_j\sigma_j\mathbf{v}_j^*, \tag{2.8}$$

where $\mathbf{u}_j$ and $\mathbf{v}_j$ are the jth columns of $\mathbf{U}$ and $\mathbf{V}$ respectively, and σ_j is the jth diagonal entry of $\mathbf{\Sigma}$.

Remark For vectorial data such as velocity, the data at one time-step are still placed in one column by considering all components of the vector.

2.3. Example: low-dimensional behaviour in cerebral and aortic aneurysm haemodynamics

2.3.1. Problem statement

Do blood flow data in aneurysms exhibit low-dimensional behaviour? How many modes are required to reconstruct

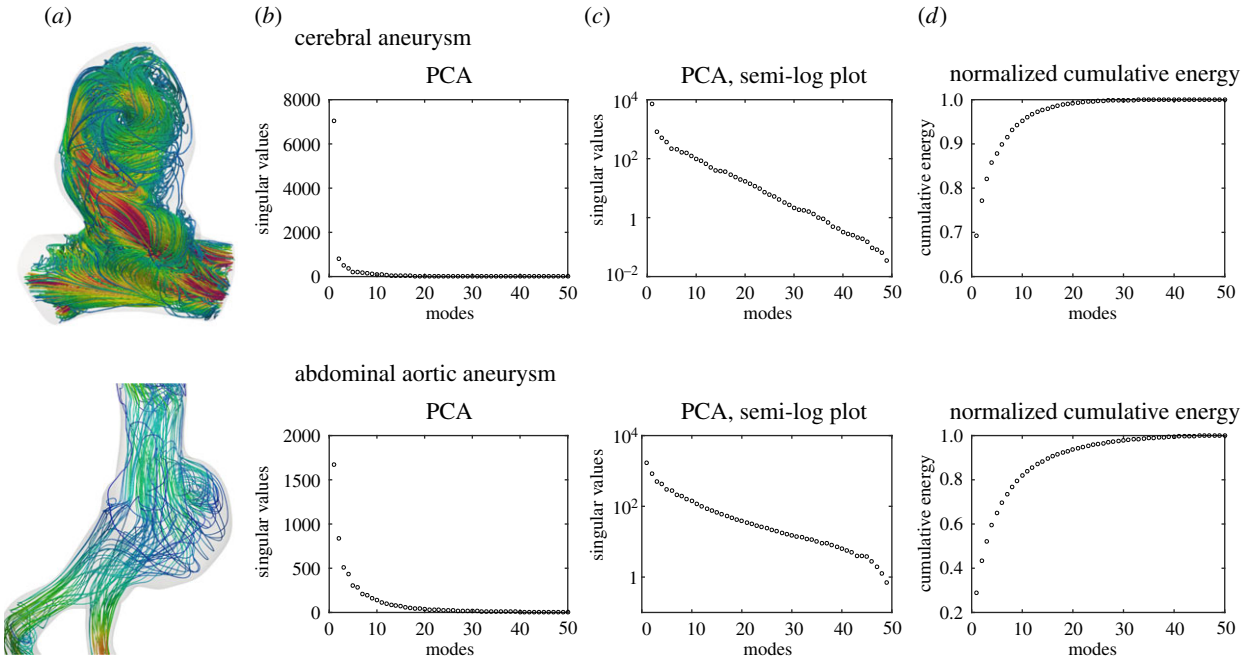

Figure 1. PCA performed on cerebral and abdominal aortic aneurysm velocity data. (*a*) A single snapshot of the velocity streamlines is shown. (*b*) The singular values for different principal components (modes) are plotted. (*c*) A semi-log plot is shown for better visualization in the range of singular values. (*d*) The normalized cumulative energy defined as the cumulative sum of singular values normalized by the sum of all singular values.

the data? How does the complexity in cerebral and abdominal aortic aneurysm (AAA) data compare?

2.3.2. Problem solution

Patient-specific CFD results from prior work in a cerebral aneurysm [39] and an AAA [40] are used. Details about the CFD simulations can be found in [39,40]. Fifty time-steps are used from one cardiac cycle and PCA is performed on the velocity data. The results are shown in figure 1. In the cerebral aneurysm model, a single mode is capable of capturing a significant portion of the data (70% energy), whereas more modes are required in the AAA data. To capture 90% of the data (based on singular values), 6 and 16 modes are required for the cerebral aneurysm and AAA models, respectively. The dominant modes are capable of explaining the majority of the data. The higher number of modes in the AAA data are due to the more complex and chaotic nature of blood flow in aortic aneurysms [41]. In practice, the number of modes is selected such that a balance between model complexity and fidelity is achieved.

2.4. Opportunities and challenges

PCA could not only be used to post-process data but it is also a powerful pre-processing step in various data-driven modelling tools, which will be discussed in the following sections. Herein, we have demonstrated how PCA reveals hidden low-dimensionality in haemodynamics data. In our example, the temporal data are stacked in columns; therefore low-dimensionality implies a high correlation between these columns of temporal data. Equivalently, these results also show that there must exist high amounts of correlation between measurements at different spatial locations. Beyond this example, it is possible to organize haemodynamics data differently. For example, if the columns represent haemodynamic data with varying different parameters (e.g. boundary conditions), then PCA can demonstrate the correlation among data with different parameters. Applying PCA to such data will enable data classification and pattern recognition, which could serve as a crucial step in machine learning. For example, linear discriminant analysis could be applied to labelled SVD/PCA modes for supervised learning and data classification [34]. This technique has been used to investigate correlations between haemodynamic and geometric parameters and aortic insufficiency and ischaemic events in the aorta of left ventricular assist device patients [42]. PCA has been used in predicting cerebral aneurysm rupture based on morphology and haemodynamics [43]. Statistical shape modelling with PCA could facilitate geometric characterization of the vasculature [44–47] and the heart [48,49]. One challenge in using PCA is that the rows need to be consistently placed in different snapshots. For instance, if the haemodynamic data in columns are based on different patients, care must be taken to ensure that the data are oriented and aligned consistently. A major limitation of the PCA method is its inherent linearity. PCA cannot effectively identify low-dimensional nonlinear patterns in the data. The advantages gained by using manifold learning and nonlinear generalizations of PCA such as kernel PCA [50], locally linear embedding [51], spectral clustering [52] and autoencoder neural networks [53] should be investigated in future work. As with all statistical data analysis methods, sufficient quantity and quality of data is required such that the results obtained from applying PCA on a given dataset converge to the results that would be obtained given an infinite amount of data [54] (unless one is only interested in the properties of the specific dataset itself). This is dependent on a variety of factors, including the number of principal components to be identified, the amount of energy contained in each principal component, the accuracy required for any ensuing analysis, the presence of any bias in the sampled data towards certain principal components and the presence of measurement noise that may be present in the data. Section 3 will discuss an extension of PCA that is explicitly designed to remove random noise from data. In general, convergence of PCA can be evaluated by testing the extent to which adding or removing data influences the

results, with convergence obtained if adding additional data does not have a tangible effect on the results of the analysis.

3. Robust principal component analysis: noisy and fluctuating data

3.1. Motivation

Noisy, fluctuating data can compromise the accuracy of PCA. Such data often result in a larger number of energetic PCA modes than what is truly needed to represent the physics of the data. The issue is pronounced in experimental data but can also exist in computational data. In experimental blood flow data, noisy and corrupt data are often inevitable. Additionally, in cases where transitional flow exists (e.g. blood flow in aneurysms [55]), high-resolution CFD solvers can capture fluctuating velocity data that may compromise the temporal statistical correlation in PCA if one is interested in mean flow behaviour. Robust principal component analysis (RPCA), as developed in [56], and recently applied to fluids data in [57] has been proposed to overcome these limitations by separating the noisy data from the rest of the data using an optimization framework.

3.2. Model theory and background

Consider the same data matrix $\mathbf{X}$ defined in equation (2.1). We assume that the noise is randomly and sparsely distributed in the data. The first step is to write $\mathbf{X}$ as the sum of a low-rank matrix $\mathbf{L}$ containing the correlated data we are interested in and a sparse matrix $\mathbf{S}$ containing the noisy/fluctuating/corrupt data:

$$\mathbf{X} = \mathbf{L} + \mathbf{S}. \tag{3.1}$$

Next, the above objective is mathematically formulated using an optimization problem

$$\min_{\mathbf{L},\,\mathbf{S}} (\mathrm{rank}(\mathbf{L}) + \|\mathbf{S}\|_0) \quad \text{s.t. } \mathbf{X} = \mathbf{L} + \mathbf{S}, \tag{3.2}$$

where *rank*($\mathbf{L}$) is equivalent to the number of non-zero singular values of $\mathbf{L}$, and $\|\mathbf{S}\|_0$ (which is not strictly a norm) denotes the number of non-zero entries in $\mathbf{S}$. Optimizing equation (3.2) is a combinatorial problem, which can typically only be solved using a non-tractable brute force method. Therefore, the problem is relaxed to a convex optimization problem, formulated as

$$\min_{\mathbf{L},\,\mathbf{S}} (\|\mathbf{L}\|_* + \lambda\|\mathbf{S}\|_1) \quad \text{s.t. } \mathbf{X} = \mathbf{L} + \mathbf{S}, \tag{3.3}$$

where $\|.\|_*$ is the nuclear norm (sum of the singular values), the non-convex l_0 pseudonorm is replaced by the convex l_1 norm, and λ is a regularization parameter controlling the level of sparsity in $\mathbf{S}$. To find $\mathbf{L}$ and $\mathbf{S}$, the above problem can be solved using the augmented Lagrange multiplier algorithm [58]. Finally, we may use the $\mathbf{L}$ matrix to perform PCA as explained in the previous section.

3.3. Example: low-dimensional behaviour in haemodynamics data with noise

3.3.1. Problem statement

Can RPCA improve low-dimensional data extraction in patient-specific AAA data with noise?

3.3.2. Problem solution

The same AAA blood flow velocity data used in the previous section are used. Noise is randomly added in space and time in 30% of the data. The value of noise is sampled from a random normal distribution with zero mean and a standard deviation equal to 10% of the maximum streamwise velocity in the data. The noise is added to all components of the velocity vector using the same distribution. PCA and RPCA are applied to both original and noisy data. The results shown in figure 2 demonstrate that PCA fails in exposing the low-dimensionality in noisy data where the singular values do not asymptote to zero. RPCA overcomes this issue and reveals the low-dimensionality in the data. An interesting observation is that RPCA applied to the original data (without noise) leads to a smaller number of dominant modes compared to PCA, due to the fact that some of the data are incorporated into the sparse matrix $\mathbf{S}$, and discarded prior to the decomposition.

3.4. Opportunities and challenges

RPCA is an excellent method to detect low-dimensionality and coherent patterns in experimental haemodynamics data where noise is inevitable. Recently, RPCA has been successfully applied to experimental PIV data of complex fluid flow [57]. Experimental cardiovascular fluid mechanics techniques such as 4D flow MRI often carry a significant amount of noisy and corrupted data. RPCA could be applied to such data to reconstruct the dominant flow structures. Additionally, RPCA has the potential to facilitate data-driven modelling techniques such as dynamic mode decomposition (DMD; see §6) that are sensitive to noise. One challenge in applying RPCA is the requirement that the corrupt data should be sparsely distributed. This requirement and sensitivity to the hyperparameter λ should be investigated in the context of cardiovascular flows in future work.

4. Compressed sensing: reconstructing high-resolution data from low-resolution sampling

4.1. Motivation

In experimental modelling of cardiovascular flows, high-resolution sampling of haemodynamics data is often not possible due to inherent limitations. However, high-resolution data are an essential part of many modelling tasks (e.g. patient-specific flow waveforms for inlet boundary conditions, spatial gradients for wall shear stress calculation). In the previous sections, we saw that high-resolution data may admit a low-dimensional sparse representation in an appropriate basis. The idea behind compressed sensing (CS) is that if we have *a priori* knowledge of such a basis, then we can reconstruct high-resolution data from low-resolution sampling. CS is a theoretical framework that solves an under-determined system of linear equations when the solution is known to be sparse. As a simple example, assume we have sampled velocity data in the aorta with a spatial resolution of 3 mm (typical 4D flow MRI resolution); however, we would like to reconstruct the data with a spatial resolution of 0.5 mm (typical CFD resolution). The only constraint here is that at the sampled MRI locations, the reconstructed data must match the 4D flow MRI data. Obviously, this is an under-determined system, meaning that the reconstruction problem has an

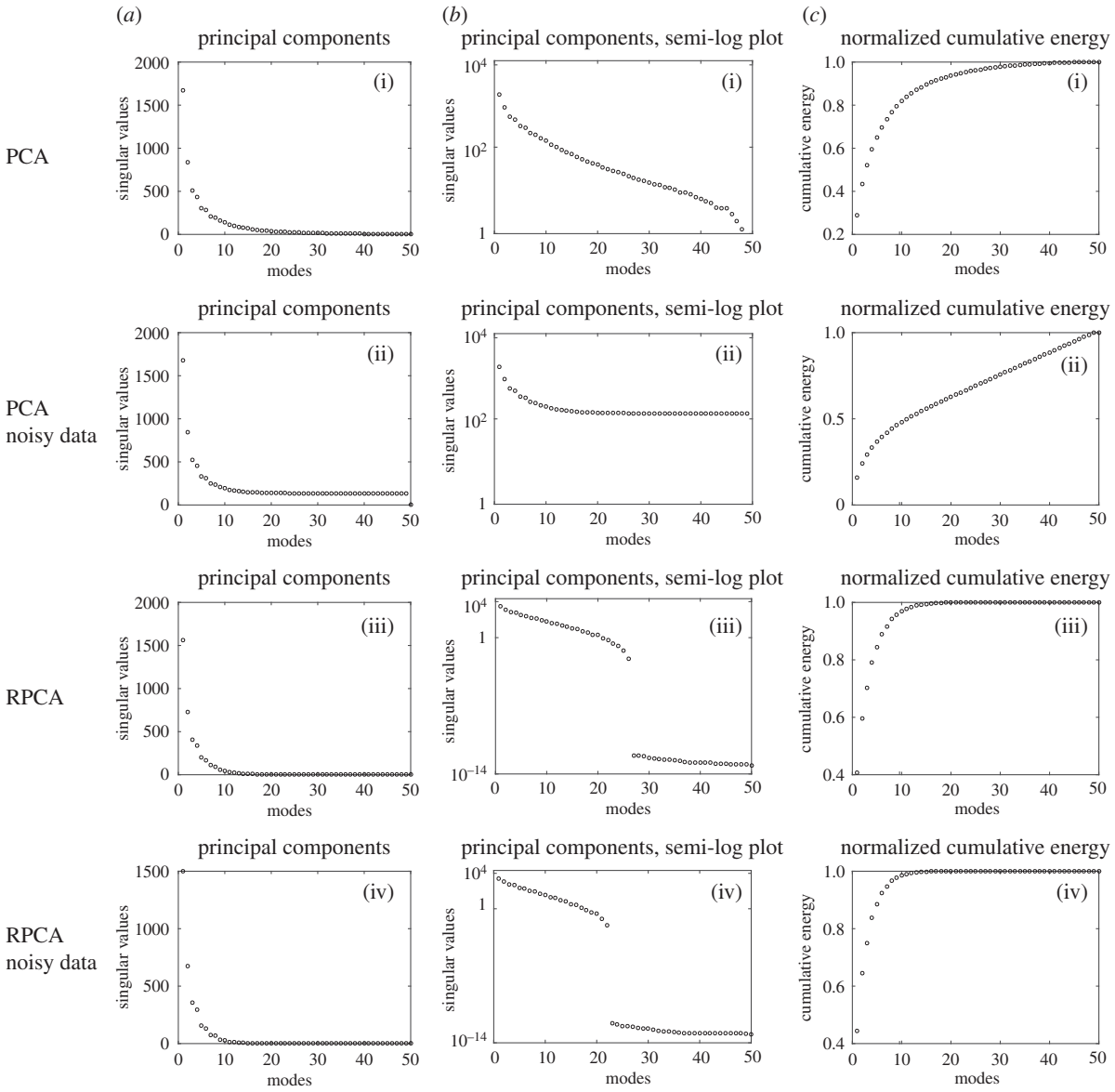

Figure 2. RPCA performed on AAA velocity data. PCA on the original data (i), PCA on the original data with noise (ii), RPCA on the original data (iii), and RPCA on the original data with noise (iv) are plotted where the principal components in (*a*) a regular plot, (*b*) semi-log plot, and (*c*) cumulative sum of singular values normalized by the sum of all singular values are shown.

infinite number of possible solutions. In CS, we regularize this problem to enable a solution, by promoting a solution that is sparse in the specified basis.

4.2. Model theory and background

Suppose we have m low-resolution measurements $\mathbf{y} \in \mathbb{R}^m$ and we want to reconstruct the high-resolution data $\mathbf{x} \in \mathbb{R}^n$ with n components, where $n \gg m$. We know the location of low-resolution measurements with respect to the high-resolution data via a known measurement matrix $\mathbf{C}$

$$\mathbf{y} = \mathbf{C}\mathbf{x}. \tag{4.1}$$

If the low-resolution measurements are a subset of the high-resolution data, then each row of $\mathbf{C}$ consists of zeros everywhere except for the column corresponding to a measurement location, which has an entry of 1. The central assumption is that we have *a priori* knowledge of a transformation $\mathbf{\Phi}$ that relates the high-resolution data with a sparse vector $\mathbf{s}$ where $\mathbf{x} = \mathbf{\Phi}\mathbf{s}$, which implies that we know how to sparsify the data. Combining the previous two equations, we arrive at an equation that could be solved for $\mathbf{s}$

$$\mathbf{y} = \mathbf{C}\mathbf{\Phi}\mathbf{s}. \tag{4.2}$$

This is an under-determined system of equations. To enable solution, the following optimization problem is solved:

$$\min_{\mathbf{s}} \|\mathbf{s}\|_1 \quad \text{s.t. } \mathbf{y} = \mathbf{C}\mathbf{\Phi}\mathbf{s}, \tag{4.3}$$

where using the l_1 norm, we seek the sparsest solution $\mathbf{s}$ that satisfies the measurement constraints. Here, the use of the l_1 norm is again used as a convex proxy for the l_0 pseudonorm representing the number of non-zero elements of $\mathbf{s}$, in order to make the problem computationally tractable. Alternatively, the optimization problem could be written using the least absolute shrinkage and selection operator method [59]

$$\min_{\mathbf{s}} \|\mathbf{y} - \mathbf{C}\mathbf{\Phi}\mathbf{s}\|_2 + \lambda\|\mathbf{s}\|_1, \tag{4.4}$$

where the hyperparameter λ controls the level of sparsity. Note in particular that this formulation means that equation (4.1) no

$$Q = a_0 + \sum_{k=1}^{3} a_k \cos(k\omega t) + b_k \sin(k\omega t)$$

a_0	a_1	b_1	a_2	b_2	a_3	b_3	ω
18.4	15.98	27.19	–26.7	18.07	–4.01	–6.18	–6.2

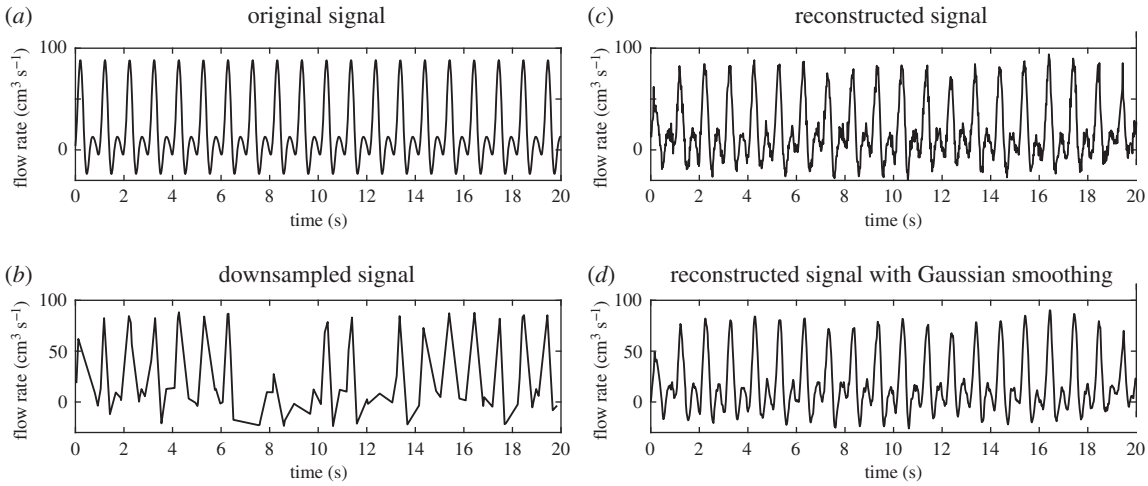

Figure 3. Pulsatile blood flow rate waveform in the infrarenal aorta is presented over 20 cardiac cycles ($T = 1$ s) using Fourier series. (*a*) The original waveform, (*b*) the downsampled waveform, (*c*) CS waveform reconstruction, and (*d*) CS waveform reconstruction with Gaussian smoothing are plotted.

longer needs to be exactly satisfied. Once $\mathbf{s}$ is found, the high-resolution data could be recovered using $\mathbf{x} = \mathbf{\Phi s}$.

4.3. Example: high-resolution reconstruction of blood flow waveform from low-resolution data

4.3.1. Problem statement

Given low-resolution measured blood flow waveform data in the aorta, is it possible to reconstruct the high-resolution flow waveform using CS?

4.3.2. Problem solution

We consider a typical blood flow waveform in the infrarenal aorta represented using Fourier series (figure 3). Such a waveform is often used as an inlet boundary condition for CFD simulations in AAAs [60]. *In vivo* phase-contrast MRI enables patient-specific measurement of such waveforms. We assume that we have low-resolution temporal sampling over 20 cardiac cycles. We randomly sample 100 data points over 20 cardiac cycles (on average 5 points per cardiac cycle). The goal is to reconstruct the data with 1000 data points (50 points per cardiac cycle). The original and downsampled waveforms are shown in figure 3*a*,*b*, respectively. In this example, we assume that the waveform is sparse in the discrete cosine transform basis. The CS solution (from equation (4.3)) is shown in figure 3*c*. The result shows significant improvement over the low-resolution data. However, the CS waveform does not perfectly recover the original waveform even though the features are recovered. Artificial high-frequency features are present in the CS recovered waveform, which may be removed using a Gaussian smoothing filter (figure 3*d*).

4.4. Opportunities and challenges

CS is a very important data-driven modelling tool with various applications [27]. In experimental cardiovascular biomechanics modelling, it is often not possible to collect data at the desired spatial and/or temporal resolution. Under certain conditions, CS provides the means to recover high-resolution data given low-resolution measurements. If we know the basis where the data are sparse, then we do not necessarily need to collect high-resolution data as we can reconstruct the data using CS. In other words, if such a basis exists, then the Nyquist–Shannon sampling law [61], which requires data sampling at a rate twice as fast as the highest frequency, is no longer required. CS is widely used in medical imaging such as computed tomography (CT) [62] and MRI [63]. For example, CS has been used to accelerate blood flow velocity measurement in 4D flow MRI in the K-space (the Fourier transform of the magnetic resonance image) [64]. However, the application of CS to high-resolution reconstruction of low-resolution blood flow data has remained elusive. A major challenge is identifying the appropriate basis where the solution is sparse. In a number of applications, sparsity in space can be achieved via a wavelet transform, while temporal sparsity can often be obtained using a Fourier transform. For example, the wavelet transform has been used to successfully reconstruct spatial data governed by the diffusion equation with 10 times higher resolution [65]. However, successful reconstruction using a standard basis will likely be challenging. Dictionary learning and transform learning provide the means to identify an optimized basis [27]; however, their success in complex blood flow data remains to be investigated. An alternative approach is to learn the sparsifying basis using training data. This topic is discussed in §7.

Another challenge is the requirement that the data should be sampled in a manner that is incoherent with the basis in which the signal is sparse. This requirement, which can be expressed more formally as the restricted isometry property [66], ensures that the sampled signal can detect non-zero coefficients of all basis elements. As a counterexample, uniform sampling is 'periodic' and thus is not incoherent with a Fourier basis. Most typically, we can allow this incoherence property to be satisfied by choosing a random sampling procedure.

5. Data assimilation using the Kalman filter: merging experimental and computational data

5.1. Motivation

Sometimes in cardiovascular flow modelling, we have the luxury of possessing both experimental data and computational models. However, both experimental and computational models have limitations and errors. Experimental data are often low-resolution and noisy, whereas even high-resolution computational simulations have limitations due to uncertainty in model parameters and/or governing equations. The field of 'data assimilation' deals with hybrid models that integrate observed experimental data with computational models. The goal is to use the computational model to advance the solution in time and based on the availability of experimental data, alter the computational model's prediction to improve solution reliability.

5.2. Model theory and background

Here, we will discuss the simplest implementation of the Kalman filter. Consider our computational model governed by a dynamical system as

$$\dot{\mathbf{x}}(t) = \mathbf{f}(\mathbf{x}, t) + \mathbf{q}_1; \quad \mathbf{x}(t_0) = \mathbf{x}_0 + \mathbf{q}_2, \tag{5.1}$$

where $\mathbf{q}_1$ is the unknown error in the model and $\mathbf{q}_2$ represents the uncertainty in the initial condition of the system. Consider the set of experimental data as

$$\mathbf{y}(t) = \mathbf{g}(t) + \mathbf{q}_3, \tag{5.2}$$

where $\mathbf{g}(t)$ are the measured data and $\mathbf{q}_3$ is the associated error. Note that the measurements do not necessarily need to be available at all points. We would like our model (equation (5.1)) to satisfy the experimental observation. The above equations form a system of overdetermined equations where we have more equations than unknowns. Therefore, an optimization problem is defined to find the solution that minimizes the error weighted by the above errors in the model and experimental data. In the case of one-dimensional data, the solution to such optimization problem may be written as

$$\bar{x}_k = x_k + K(y_k - x_k), \tag{5.3}$$

where $\bar{x}$ is the data assimilated prediction, x is the computational/analytical model, y denotes the experimental data, K is the Kalman filter (Kalman gain), and the subscript k specifies the time-step. The experimental data may not be available at every model time-step, therefore the above prediction will only be applied at the time-steps where the experimental data are available. The Kalman gain may be written as

$$K = \frac{\sigma_x^2}{\sigma_x^2 + \sigma_y^2}, \tag{5.4}$$

where it is assumed that the errors could be represented with Gaussian distributions. σ_x and σ_y represent the standard deviation of the error distribution in the model and experimental data, respectively. It could be seen that K weights the contribution of experimental and computational data based on their expected errors.

The above implementation could be extended to vectorial data and the Kalman gain could be improved and updated at every step using the extended Kalman filter method. These methods are described in a simple but informative presentation in [34] and in more detail in [25,67].

5.3. Example: merging computational and experimental trajectories in transient vortical flows

5.3.1. Problem statement

Consider an unsteady version of Hill's spherical vortex, which is an extension to the steady version that has been used as a very simple analytical model of three-dimensional vortex flows in the left ventricle of the heart [68]. The goal is to construct particle trajectories considering uncertainty in the initial condition and availability of noisy experimental data.

5.3.2. Problem solution

We extend Hill's spherical vortex [69] to a transient vortex by periodic movement of the vortex centre:

$$\mathbf{u}(x, y, z, t) = \begin{cases} (x^2 + 1 - 2r^2, \ xy, \ xz)^T & \text{if } r \le 1 \\ \left(z^2 r^{-5} - \frac{1}{3} r^{-3} - \frac{2}{3}, \ xyr^{-5}, \ xzr^{-5}\right)^T & \text{if } r > 1, \end{cases} \tag{5.5}$$

where $r = \sqrt{x^2 + (y - A)^2 + (z - A)^2}$ and $A = \sin(\pi t/50)$. The above equation is numerically integrated for $T = 20$, with the initial condition $\mathbf{x}_0 = (0, 0.5, 0)^T$ and time-step $\Delta t = 0.001$ to generate the reference data. We assume synthetic experimental data are available at a lower sampling rate ($\Delta t = 0.04$) with uncorrelated Gaussian white noise added with $\boldsymbol{\sigma}_y = 0.05$. For the computational model, we assume we do not have precise knowledge of the initial condition, and thus to each component of $\mathbf{x}_0$ we add Gaussian noise with $\boldsymbol{\sigma}_x = 0.15$. The Kalman filter method is used to correct the model prediction based on the synthetic experimental data using equation (5.3) for each component of $\mathbf{x}$, which is applied once every 40 steps (based on the lower sampling rate of the experimental data).

The results are shown in figure 4. A snapshot of the vortex flow is shown. The induced unsteadiness in the flow causes trajectory sensitivity to the initial condition. We can see that the perturbed solution (figure 4*c*) behaves very differently from the exact solution (figure 4*b*). The Kalman filter improves the estimation of the trajectory (figure 4*d*); however, noise is still present due to the noisy nature of the experimental observation. Finally, the errors in trajectories are shown (figure 4*e*) in a semi-log plot where the Kalman filter significantly outperforms the perturbed solution.

5.4. Opportunities and challenges

Herein, we have presented a very simple example of the Kalman filter. More advanced implementations of the Kalman filter are possible for more reliable results in more complex settings. For example, the ensemble Kalman filter has been used to merge 4D flow MRI and CFD simulations [70]. Parameters in zero- and one-dimensional blood flow models have been estimated based on clinical measurements using the ensemble Kalman filter [71,72] and the unscented Kalman filter [73], which are extensions formulated to deal with large state dimensions and nonlinear system dynamics, respectively. The ensemble Kalman filter has also been used to estimate the inlet flow waveform in patient-specific arterial network models [74]. Reduced-order unscented Kalman filter has been used in conjunction with fluid–structure interaction

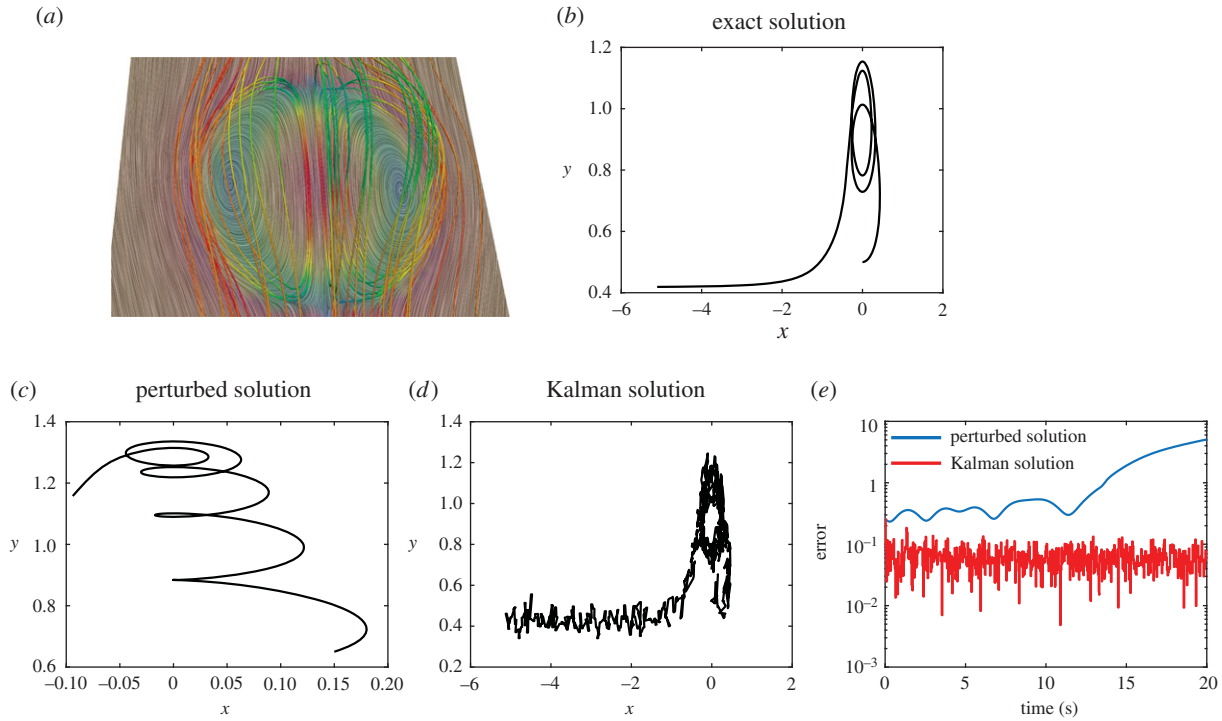

Figure 4. Data assimilation based on Kalman filter is applied to a sample trajectory from the transient version of Hill's spherical vortex. (*a*) Three-dimensional streamlines and two-dimensional streamlines in a cross-section are shown at the initial time-step. The trajectory of the (*b*) exact solution, (*c*) perturbed solution (uncertain initial condition), (*d*) Kalman filter solution are shown in the two-dimensional *x*–*y* plane. (*e*) The errors in the perturbed and Kalman filter solutions are plotted (semi-log plot).

(FSI) simulations to estimate aortic aneurysm wall stiffness from wall displacement measurements [75]. Other data assimilation methods such as variational data assimilation could also be used to merge multi-modality haemodynamics data [76]. In general, the family of Kalman filter data assimilation models provides the means to improve the accuracy of computational models by leveraging even imperfect experimental data. There are a growing number of studies in the literature on merging CFD and 4D flow MRI data using data assimilation [70,77–81]. PIV is another popular approach in haemodynamics quantification. Multi-modality data assimilation methods that leverage all of these modalities could improve the accuracy and reliability needed in transformative patient-specific haemodynamics modelling. It would be interesting to compare the relative success of all of these methods in future work. One challenge in Kalman filter modelling is the prior knowledge of the error distribution and magnitude, which might not be always available and needs to be estimated. Additionally, the assumption that errors follow a Gaussian distribution might not always be appropriate.

6. Reduced-order physics: dynamic mode decomposition and proper orthogonal decomposition

6.1. Motivation

Discovering low-dimensional behaviour in blood flow data enables a simplified understanding of the flow physics and opens up the door for efficient reduced-order and data-driven modelling. Physically, these reduced-order models are motivated by the presence of coherent structures or patterns, which are often observed in even highly complicated fluid flow processes. POD has been traditionally used in fluid mechanics for reduced-order modelling of coherent structures [5,38,82]. POD guarantees optimal reconstruction of the original dataset from an energetic perspective for a given number of modes. However, this can come with the price of losing physical interpretability due to the associated frequency mixing [83]. DMD is a more recent technique, which is data-driven (equation-free) and reduces temporal snapshots of input data to a best-fit linear reduced-order model [6,33,84,85]. POD ranks modes by energy (reconstruction optimality), whereas DMD decomposes data into modes that isolate different dynamical features within a dataset.

6.2. Model theory and background

Generally speaking, modal decomposition methods seek to decompose a system, or dataset, into spatial functions (modes), and their temporal coefficients. That is, if we have a system state given by $\mathbf{y}(x, t)$, we wish to obtain a decomposition that separates the spatial and temporal features by

$$\mathbf{y}(x, t) \approx \sum_{j=1}^{m} a_j(t)\mathbf{u}_j(x), \tag{6.1}$$

where $\mathbf{u}_j(x)$ are spatial functions, with time-varying coefficients given by $a_j(t)$. There are several methods to obtain such a decomposition from data, each of which has certain desirable features. If we wish to obtain a decomposition that is most efficient in the sense that the difference between the left and right sides of equation (6.1) is minimized, then we can utilize a singular value decomposition (i.e. PCA), as described in §2.2, using the optimality property of SVD that minimizes the reconstruction error (equation (2.6)). Here, the spatial modes $\mathbf{u}_j$ correspond to the left singular vectors of the data matrix, with the temporal functions given by the scaled right singular vectors, $a_j(t) = \sigma_j \mathbf{v}_j^*$. In this context, this is called a POD. As the

name suggests, this decomposition also gives spatial modes that are orthogonal (from the properties of SVD).

In practice, if the size of a snapshot is much larger than the number of snapshots (i.e. $n \gg m$), it can be computationally cheaper to compute this decomposition by first finding $\mathbf{v}_j$ from the eigendecomposition given in equation (2.5), from which the POD modes can be subsequently found from

$$\mathbf{u}_j = \sigma_j^{-1}\tilde{\mathbf{X}}\mathbf{v}_j. \tag{6.2}$$

This method for computing POD was first proposed in [86], and is the approach employed in the examples considered here. As discussed previously in the context of PCA, sufficient data are required to ensure that the identified POD modes are sufficiently converged. As an example, in the context of noisy experimental data, Epps & Techet [87] suggest a threshold of $\sigma_j > \epsilon\sqrt{mn}$ to ensure the accuracy of the first J modes, where ϵ is the root-mean-square noise level, and as before m and n denote the number of snapshots and size of each snapshot of data, respectively. Note also that the accuracy requirements also depend on how the results of POD are used. For example, higher quantitative accuracy may be required if the modes are used for reduced-order modelling via Galerkin projection [5], as opposed for qualitative identification of coherent structures.

POD is not the only choice of decomposition for equation (6.1). We might also want to obtain a decomposition where the coefficients $a_j(t)$ possess certain properties (note that they are also orthogonal functions in the POD). In particular, if we have

$$a_j(t) = \exp(\lambda_j t), \tag{6.3}$$

then each spatial mode can be associated with a characteristic growth/decay rate and frequency of oscillation in time, given by the real and imaginary components of λ_j, respectively. Such a decomposition can be obtained via DMD. For DMD, it is assumed that the data are time-resolved, with a fixed timestep, Δt. The fundamental idea underlying DMD is to find a linear operator $\mathbf{A}$, which maps the system one timestep into the future, the eigenvectors and eigenvalues of which are DMD modes and eigenvalues. Letting $\mathbf{X}_1$ and $\mathbf{X}_2$ denote the data matrix with the last and first column (snapshot) removed, respectively, the linear operator $\mathbf{A}$ is given by

$$\mathbf{A} = \mathbf{X}_2\mathbf{X}_1^{+}, \tag{6.4}$$

where $^+$ denotes the pseudoinverse. In practice, the $n \times n$ matrix $\mathbf{A}$ is typically not computed directly, as it is computationally easier to work in a lower dimensional space obtained via an SVD of the data. A typical algorithm to compute DMD involves the following steps:

1. Compute the (optionally truncated to rank r) SVD $\mathbf{X}_1 = \mathbf{U}\mathbf{\Sigma}\mathbf{V}^* \approx \mathbf{U}_r\mathbf{\Sigma}_r\mathbf{V}_r^*$.
2. Compute $\mathbf{A}_r = \mathbf{U}_r^*\mathbf{X}_2\mathbf{V}_r\mathbf{\Sigma}_r^{-1}$, and find its eigenvalues and eigenvectors satisfying $\mathbf{A}_r\mathbf{w}_j = \mu_j\mathbf{w}_j$.
3. Compute DMD modes $\boldsymbol{\phi}_j = \mathbf{U}_r\mathbf{w}_j$ corresponding to each continuous time eigenvalue λ_j, where $\mu_j = \exp(\lambda_j\Delta t)$.

With this approach, the number of DMD modes (or equivalently, the number of terms in the sum in equation (6.1)) is controlled by the truncation parameter, r. In practice, alternative approaches to choose a smaller number of modes can include modifying the basis of projection (e.g. [88,89]), choosing a smaller subset of modes to use from those that are computed (e.g. [90–92]), or performing a balanced truncation on the resulting linear model (e.g. [93]). There are numerous further variants of DMD that extend its applicability and usefulness for a wider variety of systems, incorporating, for example, external inputs [94], nonlinear observables [95] and noisy data [96–98]. For a more comprehensive discussion of these variants, see [15,35,93].

6.3. Example: blood flow physics in a cerebral aneurysm using dynamic mode decomposition and proper orthogonal decomposition

6.3.1. Problem statement

Given spatio-temporally resolved velocity data in a two-dimensional cerebral aneurysm model, compare the dominant DMD and POD modes.

6.3.2. Problem solution

Transient CFD simulations are performed using the open-source finite-element solver FEniCS [99]. An idealized two-dimensional cerebral aneurysm model is considered with the geometric dimensions shown in figure 5. Incompressible Navier–Stokes equations are solved with $\mu = 0.04$ P and $\rho = 1.06$ g cm^{-3}. The pulsatile inlet flow waveform is shown in figure 5 and the simulations are run for three cardiac cycles and the last cycle is used in data analysis. The mesh consists of 15.2 K triangular elements. The first four dominant POD and DMD modes are shown in figure 5. The dominant DMD modes are selected using the sparsity-promoting algorithm given in [90]. The first dominant mode in both methods is very similar. POD picks up more complex structures in the other modes, whereas the DMD modes seem to be influenced by the dominant vortex in the aneurysm.

6.4. Opportunities and challenges

Modal analysis techniques such as POD and DMD facilitate flow physics analysis by breaking down the flow evolution into several coherent structures (modes) ranked based on their energy (POD) and dynamics (DMD). These reduced-order models could also be used to reduce computational costs in simulations. However, accurate long-term extrapolation beyond the training data used in deriving these models remains a challenge. POD has been used in characterizing turbulent blood flow [100,101] and DMD has been used for quantitative modal analysis of blood flow physics [39,102]. The pulsatile nature of blood flow and variability in flow patterns during different phases of the cardiac cycle challenge the direct application of these techniques. Multistage DMD with control has been proposed to overcome these challenges in blood flow physics analysis with DMD [39].

7. Machine learning reduced-order models: overcoming uncertainty in computational models using low-fidelity experimental data

7.1. Motivation

Uncertainty in model parameters is often an inevitable aspect of patient-specific computational haemodynamics simulations. Inlet flow waveform, flow split ratio among the outlets, blood rheology, the three-dimensional geometry and vessel wall material property in FSI simulations are

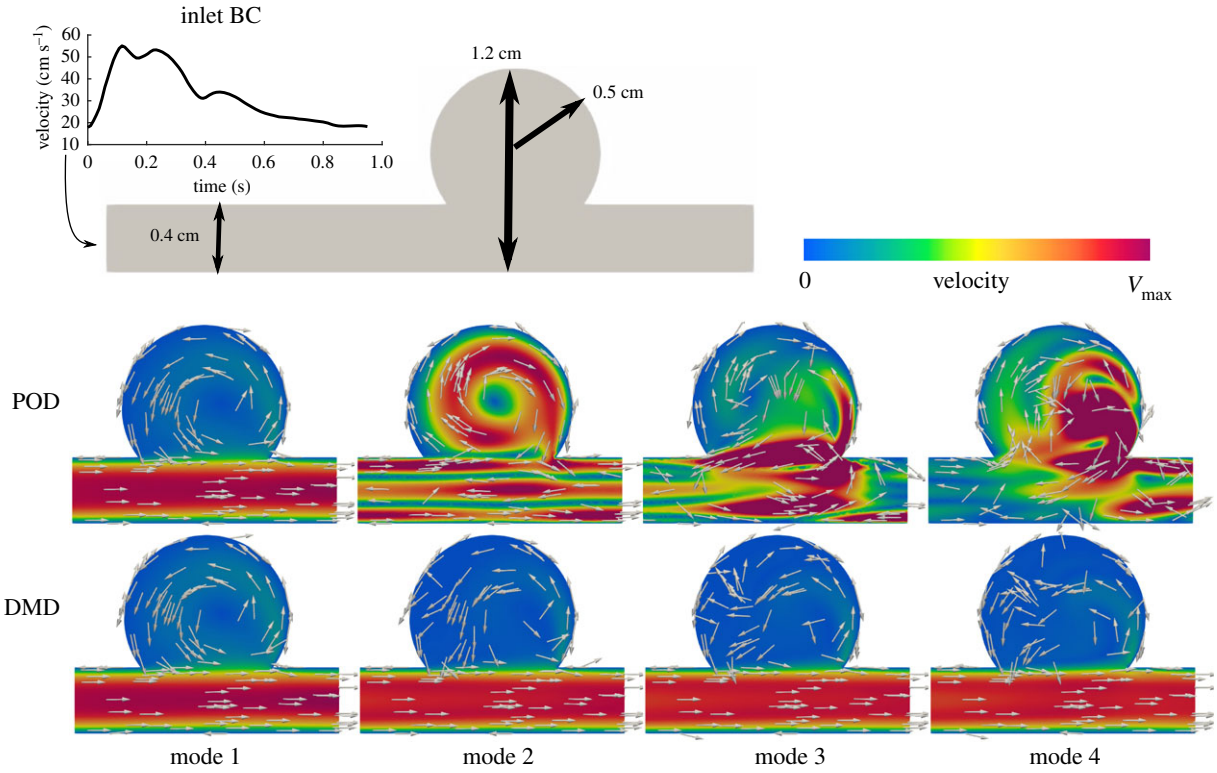

Figure 5. The first four POD and DMD modes are shown in an idealized aneurysm model with the shown geometric dimensions. The pulsatile waveform used as inlet boundary condition (BC) is shown.

often not precisely known. These uncertainties may question the fidelity of even high-resolution and minimally dissipative CFD solvers, once the results are being interpreted in the context of personalized medicine. On the other hand, *in vivo* flow measurement techniques such as 4D flow MRI do not suffer from such limitations; however, they are limited in resolution and produce noisy data. Machine learning reduced-order models provide a framework where one can construct a library of high-resolution computational simulations by varying the uncertain parameters, and couple that with reduced-order modelling and CS to reconstruct high-resolution data and identify the uncertain parameter using the low-resolution experimental data [103].

7.2. Model theory and background

First, we perform several high-resolution computational simulations by varying the uncertain parameter p times (β_1, β_2, …, β_p). Each simulation often results in several data snapshots in time. POD (equivalently, PCA) is performed on the dataset created for each parameter. Assume we need to keep m POD modes for each simulation such that we can reconstruct the data with acceptable error (e.g. capturing 99% of the energy). The number m could be different for each set of simulations, depending on the change in data complexity with variation in the uncertain parameter. A library could be constructed as

$$\boldsymbol{\psi} = \left[\, \boldsymbol{\phi}_1(\mathbf{x}, \beta_1) \;\; \cdots \;\; \boldsymbol{\phi}_m(\mathbf{x}, \beta_1) \;\; \boldsymbol{\phi}_1(\mathbf{x}, \beta_2) \;\; \cdots \;\; \boldsymbol{\phi}_m(\mathbf{x}, \beta_2) \;\; \cdots \;\; \boldsymbol{\phi}_1(\mathbf{x}, \beta_p) \;\; \cdots \;\; \boldsymbol{\phi}_m(\mathbf{x}, \beta_p) \,\right]. \tag{7.1}$$

This library contains a reduced-order representation of all possible dynamics in the system within the range of the considered parameters and may be thought of as a supervised machine learning step. Note that it is possible to perform POD just once on the entire appended dataset as opposed to each β parameter. This approach could still be used for data reconstruction; however, it will make parameter identification less trivial. Next, an underdetermined system of equations is constructed as $\hat{\mathbf{Y}} = (\mathbf{C}\boldsymbol{\psi})\mathbf{b}$, where $\hat{\mathbf{Y}}$ is the low-resolution experimental data, $\mathbf{C}$ is a measurement matrix specifying measurement locations, and $\mathbf{b}$ is a vector to be determined. To find the solution, the following CS problem is solved (see §4):

$$\min_{\mathbf{b}} \|\mathbf{b}\|_1 \text{ s.t. } \hat{\mathbf{Y}} = (\mathbf{C}\boldsymbol{\psi})\mathbf{b}. \tag{7.2}$$

To enable CS, the measurement locations used ($\mathbf{C}$) should be randomly selected. As we discuss in example 2, relaxing the CS optimization problem can perform better in parameter identification

$$\min_{\mathbf{b}} \|\mathbf{b}\|_1 \text{ s.t. } \|\hat{\mathbf{Y}} - (\mathbf{C}\boldsymbol{\psi})\mathbf{b}\|_2 < \epsilon, \tag{7.3}$$

where ϵ is a tolerance. Once the above optimization problem is solved, the high-resolution data are reconstructed as $\mathbf{Y} = \boldsymbol{\psi}\mathbf{b}$.

Thus far, we have not specified the locations of measurements (as defined by $\mathbf{C}$). Additionally, we have assumed knowledge of a basis in which our data are sparse, but have not prespecified which basis elements will have non-zero coefficients (i.e. which terms in $\mathbf{b}$ are non-zero). Here, following the work of [13], we show that favourable

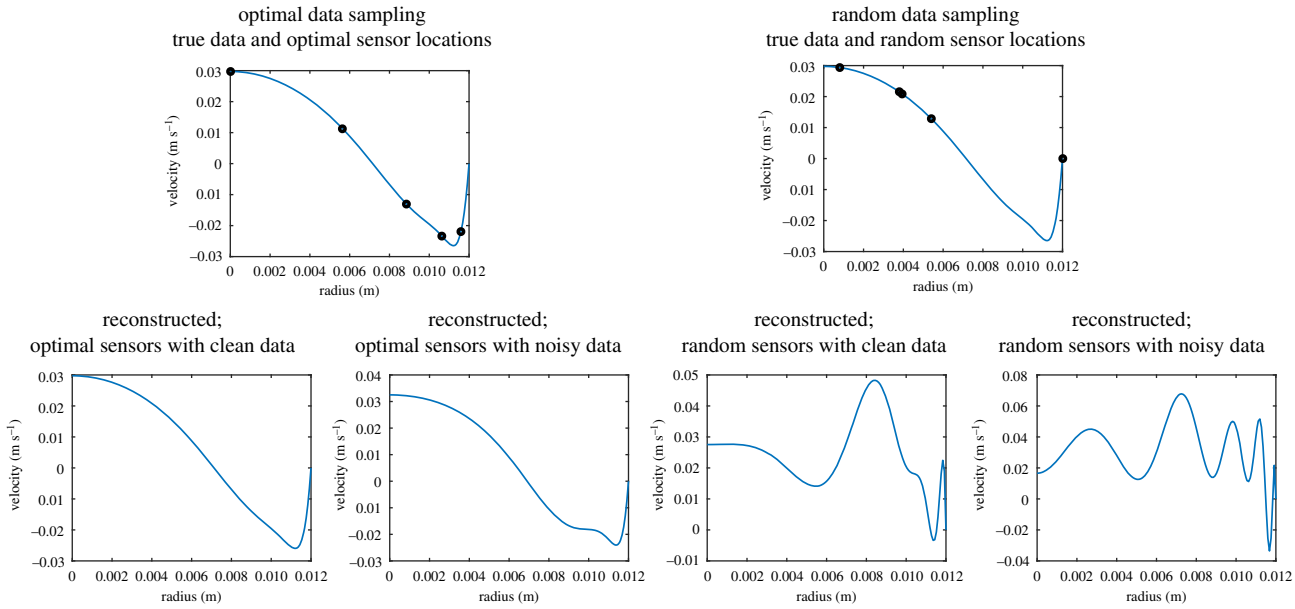

Figure 6. The groundtruth velocity profile is shown with optimal (left) and random (right) sampling. For each case, the reconstructed velocity profile under clean and noisy data is shown.

sensor/measurement locations can readily be found given knowledge of such basis elements. From §2.2, a low-dimensional set of functions that capture most of the original data may be obtained from the columns of $\mathbf{U}_r$ in the truncated SVD

$$\boldsymbol{\psi} = \mathbf{U}\boldsymbol{\Sigma}\mathbf{V}^* \approx \mathbf{U}_r\boldsymbol{\Sigma}_r\mathbf{V}_r^*, \tag{7.4}$$

where $\mathbf{U}_r$ and $\mathbf{V}_r$ denote the first r columns of $\mathbf{U}$ and $\mathbf{V}$, and $\boldsymbol{\Sigma}_r$ contains the first r diagonal entries of $\boldsymbol{\Sigma}$. Under the assumption that $\boldsymbol{\psi} \approx \mathbf{U}_r\mathbf{U}_r^*\boldsymbol{\psi}$, we can, in theory, reconstruct the high-resolution data from r measurement locations by solving the (no longer underdetermined) equation

$$\hat{\mathbf{Y}} = \mathbf{C}\mathbf{U}_r(\mathbf{U}_r^*\boldsymbol{\psi}) = \mathbf{C}\mathbf{U}_r\mathbf{a}, \tag{7.5}$$

where the r-dimensional vector of coefficients $\mathbf{a} = \mathbf{U}_r^*\boldsymbol{\psi}$. In principle, equation (7.5) can be solved for $\mathbf{a}$ for any choice of sensor locations $\mathbf{C}$ that give linearly independent equations, by using the pseudoinverse

$$\mathbf{a} = (\mathbf{C}\mathbf{U}_r)^+\hat{\mathbf{Y}}. \tag{7.6}$$

However, some choices of $\mathbf{C}$ can result in these equations being ill-conditioned, which means in particular that noisy measurements $\hat{\mathbf{Y}}$ can give wildly inaccurate reconstructions of the full data. One method to select measurement locations, as described in [13], is to choose sensor locations in a manner that results in $\mathbf{C}\mathbf{U}_r$ having a small condition number. This can be achieved via the pivoted QR decomposition

$$\mathbf{U}_r^T\mathbf{C}^T = \mathbf{Q}\mathbf{R}, \tag{7.7}$$

where the permutations in $\mathbf{C}^T$ ensure that the diagonal elements of $\mathbf{R}$ are ordered from largest to smallest. In the examples below, we call this approach optimal sampling. Similar data reconstruction methods are used in the empirical interpolation methods described in [11,12,104]. To summarize, application of this method involves:

1. Obtain a set of modes/functions $\mathbf{U}_r$ that sufficiently capture the high fidelity data (e.g. via an SVD).
2. Find optimal measurement locations (e.g. low-dimensional data) using a pivoted QR decomposition of $\mathbf{U}_r$ (equation (7.7)).
3. Find the mode coefficients $\mathbf{a}$ from equation (7.6).
4. Reconstruct the high-fidelity data via $\mathbf{Y} = \mathbf{U}_r\mathbf{a}$.

7.3. Example 1: reconstruct high-resolution Womersley flow with uncertain Womersley number and optimal sensor placement

7.3.1. Problem statement

Given a few clean or noisy velocity samples from the Womersley flow profile, is it possible to reconstruct the entire velocity profile without knowing the Womersley number?

7.3.2. Problem solution

For demonstration purposes, we consider a wide range of Womersley numbers α (1–29) based on a fixed pressure gradient waveform (reported in [39]) to construct a library of Womersley velocity profiles based on Womersley's analytical solution [1]. The data are based on 150 radial locations and 100 time-steps over one cardiac cycle. In this example, in constructing the library, we apply POD once to the entire data. The reference data (groundtruth) are considered to be $\alpha = 14.7$. To test how the method works under noise, noisy data are created by adding random Gaussian noise with zero mean and standard deviation of 10% the maximum velocity. Given only five random and optimal sample points along the radial direction at one time-step, we are interested in reconstructing the velocity profile. The results are shown in figure 6. Optimal sensor placement can reconstruct the true data with high accuracy (l_2 norm in error 0.03 and 0.002 for noisy and clean data, respectively). Data reconstruction with random sensor placement has difficulty in reconstructing the data (l_2 norm in error 0.45 and 0.35 for noisy and clean data, respectively). More sampling points are required for successful reconstruction with random sampling, and the optimal sensor placement method is more robust to noise.

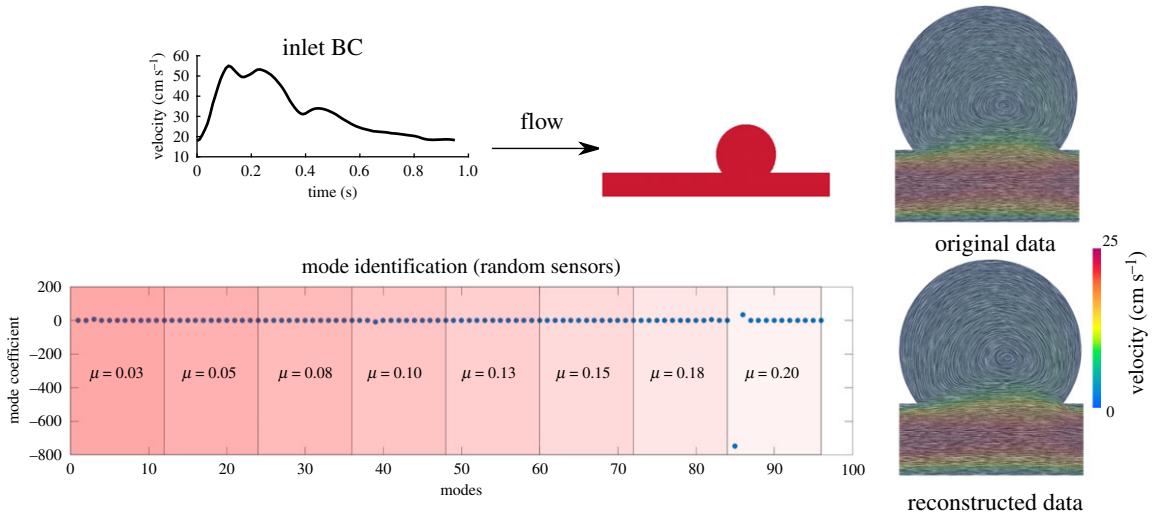

Figure 7. The two-dimensional aneurysm model and inlet boundary condition (BC) for CFD simulations are shown. The velocity streamlines for the original and reconstructed data are shown. The time-point of the original data is marked with a red dot in the waveform. The mode coefficients in the reduced-order model library are plotted. The method correctly identifies the dominant mode as being associated with the set of $\mu = 0.2$ P modes. The measurement sensors were randomly placed.

7.4. Example 2: reconstruct high-resolution cerebral aneurysm flow with uncertain viscosity

7.4.1. Problem statement

Patient-specific variation in blood viscosity is common in patients with haemorheological disorders (e.g. diabetes) [105]. Given sparse (low-resolution) sampling of noisy velocity data in a two-dimensional cerebral aneurysm flow with an unknown viscosity, is it possible to identify the viscosity?

7.4.2. Problem solution

The two-dimensional cerebral aneurysm model in §6 is considered. Simulations are performed for eight different dynamic viscosity values uniformly distributed between $\mu = 0.03$ and 0.2 P. Spatio-temporal velocity data are collected for all μ values. We consider $\mu = 0.2$ P as the groundtruth data. Additionally, we assume we only have one temporal snapshot inside the cardiac cycle available for measured data. In this example, we consider 150 random data samples (sensors) to collect two-dimensional velocity vector data. Noisy data are created by adding Gaussian noise with zero mean and standard deviation of 5% the velocity data at each location. POD is performed for each parameter and appended to build the library $\boldsymbol{\psi}$ by keeping 12 modes for each parameter. The relaxed version of the CS problem (equation (7.3)) is solved to identify the active modes in the library and reconstruct the data. Parameter identification is done based on the dominant active modes in the library. The resulting active modes are shown in figure 7. The dominant active mode belongs to the set of modes where $\mu = 0.2$ P, and therefore the method correctly identifies the unknown viscosity. Most of the other modes are close to zero in accordance with the sparse regression model. The reconstructed velocity patterns are very close to the original data. In general, further investigation showed that parameter identification could be achieved with fewer sensors, whereas accurate data reconstruction required more sensors. For example, with even 30 sensors the algorithm was capable of correctly identifying the unknown viscosity (with reduced reconstruction accuracy). Another important observation is the sensitivity of the CS algorithm to noise. In the presence of noise, the relaxed version of the optimization problem (equation (7.3)) with a relatively high value of ϵ was required for convergence (herein, ϵ was set to 25% of the maximum velocity). In the example considered here, an increase in ϵ increased reconstruction error as expected but did not affect parameter identification.

7.5. Opportunities and challenges

The machine learning ROM framework is capable of merging high-resolution numerical data (with an uncertain parameter) with low-resolution experimental data. A promising application is overcoming limitations in patient-specific CFD and 4D flow MRI characterization of haemodynamics. In CFD modelling, we can generate high-resolution data but often have to face uncertainty in parameters and assumptions. On the other hand, *in vivo* 4D flow MRI directly measures blood flow inside the body (without uncertainty in parameters); however, it is subject to imaging artefacts and noise. The machine learning ROM approach could provide a method to overcome these limitations. A similar framework has been used to merge CFD and 4D flow MRI where the authors assumed uncertainty in the CFD inlet flow waveform [78]. The machine learning ROM method could be extended to scenarios where multiple uncertain parameters are present. One challenge in merging CFD and 4D flow MRI data is the discrepancy in geometries during image segmentation and three-dimensional model creation, which could be thought of as another uncertain parameter (the wall location where the no-slip boundary condition is imposed). It might be possible to use the machine learning framework in conjunction with non-uniform rational basis spline surfaces (e.g. isogeometric finite element analysis [106]) to have control over a set of parametrized geometries. Another challenge is the construction of the training library, which is the computationally expensive part of the model. Greedy algorithms that can appropriately identify the set of parameters in the library construction process could mitigate this difficulty [107].

8. Low-rank data recovery from random spatio-temporal measurements

8.1. Motivation

In the previous sections, to reconstruct high-resolution data, we needed prior knowledge of a basis where the data were sparse. Such knowledge might not always be available. However, if the data matrix (equation (2.1)) is low-rank, then the full data could be recovered with partial data sampling using low-rank matrix recovery [27]. A low-rank matrix implies that most of the columns of the matrix (herein, temporal snapshots) are not linearly independent. In other words, the total degree of freedom of the matrix is much smaller than the total number of entries; therefore, we may hope to be able to reconstruct the full data with partial observation. In complex cardiovascular flows, given a large number of spatial data points (number of rows) and the complexity in the flow, perfectly correlated columns might not be observed. For instance, noise in data either due to measurement or numerical errors will cause the data matrix to be full rank. Nevertheless, a high correlation in temporal snapshots is often observed in haemodynamics data. As shown below, the low-rank matrix recovery method could also work under these scenarios. Therefore, given low-resolution random spatial and temporal sampling of haemodynamics data, we might be able to reconstruct the full data.

8.2. Model theory and background

Consider the data matrix $\mathbf{X}$ in equation (2.1). Assume we only observe a random subset of entries (Ω) in the matrix (random spatial and temporal sampling of data). Our goal is to reconstruct the entire matrix $\mathbf{X}$ with such observation assuming that $\mathbf{X}$ is low rank. Namely,

$$\min \text{rank}(\mathbf{X}) \text{ s.t. } \mathbf{Y} = M_{\Omega}(\mathbf{X}), \tag{8.1}$$

where M_{Ω} is a masking operator that selects the entries of $\mathbf{X}$ that have been observed as $\mathbf{Y}$. This optimization problem is computationally very expensive to solve (non-deterministic polynomial hard). However, the problem could be relaxed to a convex optimization problem

$$\min \|\mathbf{X}\|_{*} \text{ s.t. } \mathbf{Y} = M_{\Omega}(\mathbf{X}), \tag{8.2}$$

where $\|.\|_{*}$ is the nuclear norm, in a similar manner to the 'convexification' employed for robust PCA in §3.2. This could be solved using the singular value shrinkage algorithm [27].

8.3. Example: reconstruct high-resolution blood flow with random spatio-temporal measurements

8.3.1. Problem statement

Given low-resolution spatio-temporally random sampling of blood flow velocity data in a cerebral aneurysm and a coronary artery stenosis, is it possible to recover the high-resolution data?

8.3.2. Problem solution

Consider the pulsatile blood flow problem in the two-dimensional idealized cerebral aneurysm problem in §6.3 and a three-dimensional coronary artery stenosis model from a prior study [39]. We collect the velocity data in the aneurysmal and plaque regions (boxed regions in figure 8) and stack the spatio-temporal velocity data into the data matrix $\mathbf{X}$ similar to equation (2.1). The collected data include vectorial velocity data at 3943 spatial locations and 49 time-steps throughout the cardiac cycle for the two-dimensional aneurysm model and 73 239 spatial locations and 51 intra-cardiac time-steps for the three-dimensional coronary artery model. Using the low-rank matrix recovery method, we reconstruct the full data given only 10% and 40% random spatio-temporal sampling of the data matrix. The results for two points are shown in figure 8. We observe that 40% sampling can perfectly capture the velocity outside the aneurysm and with mostly low error for the point inside the aneurysm and coronary artery stenosis regions. With 10% sampling, the algorithm can still perform well for the point outside of the aneurysm with errors near the peak flow rate, whereas the performance for the point inside the aneurysm and stenosis where more complex flow is present is not as good.

8.4. Opportunities and challenges

Matrix completion algorithms provide a promising tool to complete the data when random measurements are missing and a high correlation exists within the data. Similar ideas have been used in reconstructing statistics in turbulent flows [108]. In the context of cardiovascular flows, often the data are correlated, and therefore we may use matrix completion algorithms to increase the spatio-temporal resolution. Interestingly, we observed that the algorithm can successfully complete the data matrix even if the matrix was full-rank, but exhibited low-rank behaviour once the threshold used in defining the matrix rank was relaxed. One challenge in such methods is the requirement that the incomplete data sampling should be random (in space and time). However, it might be possible to draw random samples from a uniform sampling to be able to use such methods. Of course, such random samplings need to be carefully devised to avoid accuracy loss.

9. Sparse identification of nonlinear dynamics: discovering analytical dynamics

9.1. Motivation

Extracting analytical governing equations from large datasets has the potential to simplify our physical understanding of dynamical systems and facilitate modelling. Sparse identification of nonlinear dynamics (SINDy) is a recent paradigm that enables the discovery of governing equations from data [7]. The central assumption is that the governing equations can be selected sparsely given an appropriately chosen set of candidate functions.

9.2. Model theory and background

Consider a nonlinear dynamical system

$$\dot{\mathbf{x}}(t) = \mathbf{f}(\mathbf{x}), \tag{9.1}$$

where $\mathbf{x}(t)$ is the state of the system (e.g. particle position in fluid flow) as a function of time and $\mathbf{f}$ is the dynamics of the system that we would like to approximate analytically and sparsely using a few functions. We consider a library

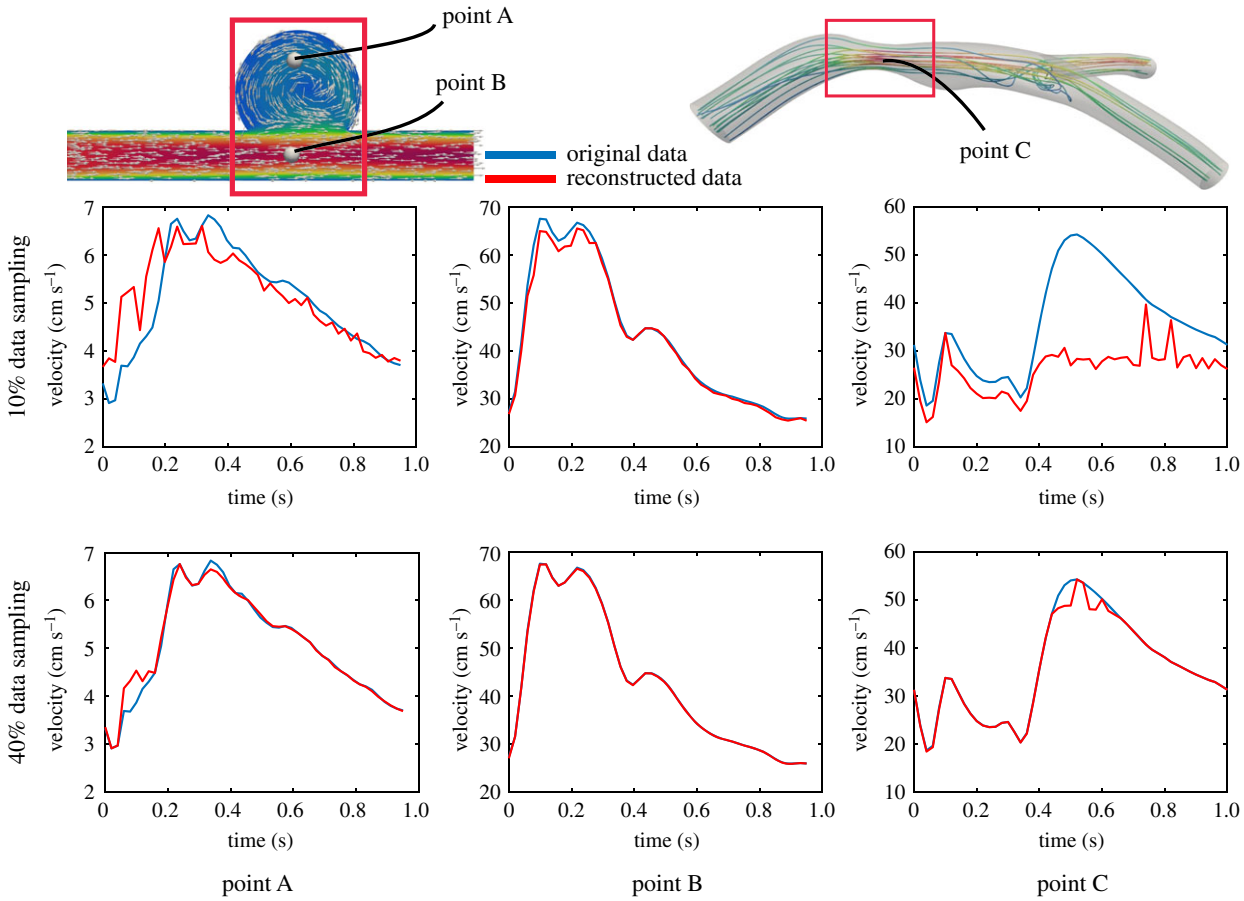

Figure 8. Velocity data are reconstructed in a two-dimensional cerebral aneurysm and a three-dimensional coronary artery stenosis model from random spatio-temporal sampling of the data and using low-rank matrix recovery. The boxed region shows the region of interest where the data analysis is performed. The data are reconstructed at point A (inside the aneurysm), point B (inside the parent artery in the aneurysm model) and point C (in the plaque region of the coronary artery model) using 10% and 40% random spatio-temporal sampling. The velocity results are plotted versus time where the red line is the reconstructed data and the blue line is the original data.

of candidate functions

$$\Theta(\mathbf{X}) = \begin{bmatrix} \vdots & \vdots & \vdots & \vdots & \vdots & \vdots & \vdots \\ 1 & \mathbf{X} & \mathbf{X}^{P_2} & \mathbf{X}^{P_3} & \cdots & \sin(\mathbf{X}) & \cdots \\ \vdots & \vdots & \vdots & \vdots & \vdots & \vdots & \vdots \end{bmatrix}, \tag{9.2}$$

where $\mathbf{X}^{P_2}$ is the set of quadratic nonlinear functions combining the state vector (e.g. $x_1(t)^2$, $x_1(t)x_2(t), \ldots$) and so forth. Subsequently, we represent our dynamical system (equation (9.1)) with these functions

$$\dot{\mathbf{X}}(t) = \boldsymbol{\Theta}(\mathbf{X})\boldsymbol{\Xi}, \tag{9.3}$$

where each column of the matrix $\boldsymbol{\Xi}$, ζ_k is a sparse vector of coefficients that determines the active functions in $\boldsymbol{\Theta}$. To find ζ_k and therefore the active functions, a convex optimization problem such as the following can be solved:

$$\min_{\zeta_k} \|\dot{\mathbf{x}}(t) - \boldsymbol{\Theta}(\mathbf{X})\zeta_k\|_2 + \lambda\|\zeta_k\|_1, \tag{9.4}$$

where the λ term promotes sparsity in the selected coefficients. In practice, the identification of the coefficients ζ_k can instead be solved using a sequential thresholded least-squares algorithm to improve performance under noisy data [7]. Finally, the governing equations for the dynamical system could be written for each state x_k as

$$\dot{x}_k(t) = \boldsymbol{\Theta}(\mathbf{X})\zeta_k. \tag{9.5}$$

9.3. Example 1: discover a blood coagulation and thrombosis model

9.3.1. Problem statement

Modelling the fluid mechanics of thrombosis (blood clot formation) requires solving large systems of advection–diffusion–reaction equations. It is highly desirable to identify reduced-order thrombosis models from data to simplify thrombosis simulations [109]. Given the temporal evolution of the prominent biochemicals involved in thrombosis, is it possible to identify the governing equations for the reaction kinetics?

9.3.2. Problem solution

We consider the reduced-order thrombosis model of Papadopoulos [110,111] shown in figure 9. The system of ordinary differential equations models the biochemical reaction kinetics involved between thrombin (IIa), prothrombin (II), activated platelets (AP) and resting platelets (RP). First, we eliminate the resting platelets from the system by realizing that the [AP] + [RP] is constant. This is an essential step since the SINDy algorithm performs poorly when some variables are highly correlated, due to $\boldsymbol{\Theta}$ becoming ill-conditioned. The reduced Papadopoulos model is solved to generate biochemical trajectories. In real practice, these trajectories come from experimental data or high-dimensional thrombosis models and the goal is to identify the governing

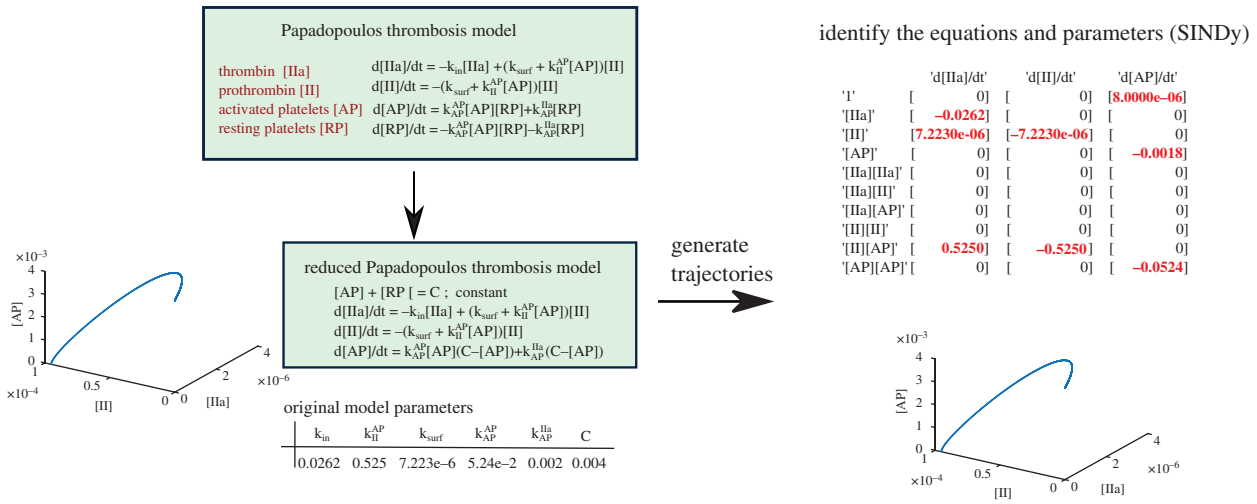

Figure 9. The SINDy algorithm is applied to the Papadopoulos thrombosis model to identify the equations from data. First, a reduced version of the Papadopoulos model is derived by eliminating the activated platelets [AP] using [AP] + [RP] = C where C = 0.004 is determined from the initial conditions ($[IIa]_0 = 0$, $[II]_0 = 9.509 \times 10^{-5}$, $[AP]_0 = 0$, $[RP]_0 = 0.004$). The constructed trajectories ([IIa](t), [II](t) and [AP](t)) are used to identify the original governing equations using the sparse regression in SINDy.

equations for the reaction kinetics based on these trajectories. In constructing the library $\boldsymbol{\Theta}$, the set of all linear and quadratic functions (based on state variables) are considered. Given the current model, considering a broader set of linearly independent functions did not affect the results. The original model, the generated trajectory, and the identified equations and trajectory from SINDy are shown in figure 9. Using the solution trajectories, SINDy exactly captures the active terms and coefficients in the governing equations.

9.4. Example 2: discover analytical velocity in transient vortical flows

9.4.1. Problem statement

Given particle trajectories in an unsteady three-dimensional vortical flow, is it possible to estimate the time-dependent velocity vector field using SINDy?

9.4.2. Problem solution

We consider a modified version of the unsteady Hill's spherical vortex in §5.3 where the three-dimensional velocity field is given by

$$\begin{cases} u(x, y, z, t) = x^2 + 1 - 2r^2 = 0.75 + 0.25\cos(4\omega t) \\ \quad - x^2 - 2y^2 - 2z^2 + 2y\sin(2\omega t) \\ v(x, y, z, t) = xy \\ w(x, y, z, t) = x(z + 0.4\sin(2\omega t)), \end{cases} \tag{9.6}$$

where $\omega = \pi/100$ and $r = \sqrt{x^2 + (y - 0.5\sin(2\omega t))^2 + z^2}$. We simulate particle transport for 8 seconds under this flow for a particle with the initial position of $(x_0, y_0, z_0) = (0.02, 0.05, 0.01)$. Given the resulting trajectory $(x(t), y(t), z(t))$, we would like to find an analytical representation for the velocity field. Here, we use SINDy with control (SINDYc) [112] as a simple extension of the SINDy algorithm to be able to estimate time-dependent dynamical systems. For the library Θ, the set of all linear and quadratic functions in x,y,z as well as $\sin(j\omega t)$, $\cos(j\omega t)$, $x_i\sin(j\omega t)$, $x_i\cos(j\omega t)$ are considered where $j = 1, 2, \ldots, 5$, and $x_i = x, y, z$. For simplicity, we have assumed prior knowledge about ω; however, it is possible to consider a wide range of frequencies by expanding the library. The results are shown in figure 10. Comparing the active velocity terms and coefficients with equation (9.6), we see that the correct terms are accurately predicted.

9.5. Opportunities and challenges

We have demonstrated two examples of SINDy that could be used in cardiovascular flow modelling. Systems biology models (system of ordinary differential equations governing biological reaction kinetics) are an essential part of multiscale mechanobiology models of disease growth [113,114]. SINDy provides a framework to derive such models from experimental data or identify reduced-order systems biology models from higher-order models. Identifying analytical velocity fields from particle trajectories is another example. Of course, this is expected to be a challenging task in complex cardiovascular flows. We have shown an example based on an idealized vortex flow. It remains to be investigated if similar models could be derived from other vortex-dominated flows such as blood flow in the left ventricle. One challenge in the application of SINDy is that the matrix Θ becomes ill-conditioned once the trajectories are highly correlated, which will compromise the algorithm results. A reweighted l_1 regularized least squares technique has been proposed to overcome this issue [115]. Another challenge is in building the library of candidate functions. In the examples considered, not considering an important active term in the library resulted in a dense solution where most terms became active. It should be noted that depending on the complexity of the system studied, it may not always be possible to represent a dynamical system sparsely. Finally, SINDy has been extended to partial differential equations (PDE) to identify active terms and coefficients in spatio-temporal PDE models [116].

10. Other techniques and applications

In this section, we briefly discuss some of the recent trends in data-driven modelling and data science and their potential in cardiovascular flow modelling.

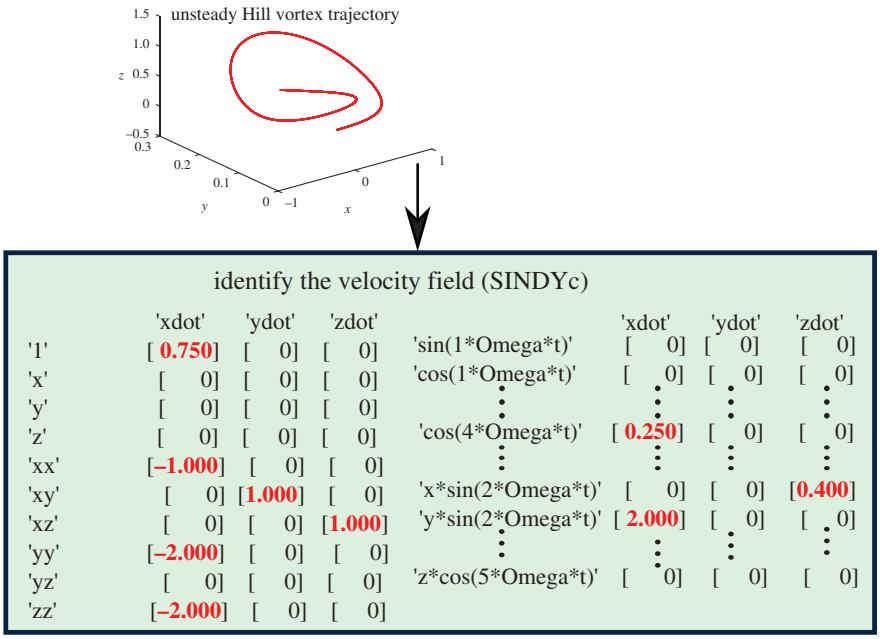

Figure 10. The SINDy with control (SINDYc) algorithm is applied to a particle trajectory generated from an unsteady version of Hill's spherical vortex. The particle trajectory is plotted and the terms identified for the velocity vector field from SINDYc are listed. SINDYc exactly captures the correct terms.

10.1. Machine learning and neural networks

Neural networks are a powerful class of machine learning techniques and may be thought of as an approximator to complex nonlinear functions. A popular application in cardiovascular research is learning clinical outcomes based on different input parameters derived from patient-specific simulations [117,118]. We may think of this as an advanced multi-parameter regression framework where we have several input parameters, different clinical outcomes, and large databases where we are interested in learning/fitting a statistical relationship between the data, which is achieved through the learning process. Another application area is learning models from complex large datasets. An active area of research related to this is learning turbulence models based on direct numerical simulation (DNS) databases [119]. Given the unique physics of turbulence in cardiovascular flows [120,121], learning customized Reynolds averaged Navier–Stokes or large-eddy simulation models based on high-fidelity DNS data of turbulent pulsatile blood flow seems to be a promising area of future research. A common question for machine learning is if it can replace physics-based cardiovascular flow simulations, and therefore provide a very fast patient-specific estimation of haemodynamics once the one-time expensive training process is completed. Currently, this paradigm has been successfully used to estimate CFD-based fractional flow reserve (FFR) in coronary artery stenosis [122]. However, FFR is a single variable that measures the reduction in flow rate (pressure drop) due to a stenosis. Using a similar paradigm for estimating variables that exhibit spatial and temporal variation (e.g. velocity or wall shear stress) [123] is a much more involved process, in which extremely large datasets are required, and it is not clear if it could be achieved in the near future. In fact, even large datasets are likely not 'large' enough when it comes to systems that are highly sensitive to variations in input data [124]. The recent physics-informed neural networks (PINN) paradigm [125] considers the governing equations in the learning process and could ultimately reduce some of the costs associated with traditional CFD modelling such as mesh creation. PINN has been used for an example inverse modelling problem in cardiovascular flows where one is interested in estimating the velocity field based on concentration data [126]. This approach seems to pave the way to a new *in vivo* framework for measuring velocity based on time-resolved concentration measured using medical imaging (e.g. dynamic contrast-enhanced imaging). Finally, PINNs have been recently used for improving 4D flow MRI data fidelity (super-resolution and denoising) [127].

10.2. Parametric reduced-order models

The reduced-order models that we discussed in §6 did not consider parameter variation. Namely, we approximated them given spatio-temporal velocity data for a fixed parameter. Sometimes in computational modelling, we are interested in a range of parameters. Reduced-order modelling tools such as the Galerkin-POD learn a projected space and basis, which they use to evolve the solution and therefore provide a computationally efficient prediction of the solution. These methods are trained based on fixed parameters and therefore cannot be used when parameters in the model change. Parametric reduced-order models have been developed to address this challenge [107,128]. These reduced-order modelling techniques could be valuable in multiscale modelling of cardiovascular disease growth where parameters in the blood flow or structural mechanics models can change during disease growth simulation.

10.3. Data-driven multiscale modelling

Multiscale modelling of cardiovascular disease is challenging as such models need to connect different models across different spatial and temporal scales. Data-driven modelling and machine learning have the potential to transform multiscale modelling of cardiovascular disease [129].

Reduced-order models can be used to accelerate computationally expensive multiscale models. We may use the data generated from expensive multiscale simulations or experimental observations to derive a simplified approximation of the underlying physics (e.g. using SINDy). Complete collection of biological data across multiple scales represents a major challenge in calibrating parameters in multiscale models. Developing data-driven multiscale models that can leverage sparsity or are robust to corrupt and incomplete data is a promising topic of future research. In prior sections, we discussed data-driven modelling with multi-modality data. Developing multiscale models that can appropriately leverage multi-modality data is another interesting topic [130]. Deep neural networks provide a promising framework for multiphysics and multiscale modelling [131]. Combining data-driven modelling and machine learning with physics-based simulations provides a hybrid modelling strategy [132] with high potential in multiscale modelling of biological systems [129]. Advancements in each of these fields and their coupling will produce predictive digital twins [133] that could facilitate treatment planning, patient management and ultimately transform personalized cardiovascular medicine [134].

11. Conclusion

Recent advances in computational power, data science and abundance of data are starting to revolutionize different fields of science and engineering. Data-driven cardiovascular flow modelling is currently at its infancy, yet there are various opportunities to develop customized data-driven models that can transform cardiovascular biomechanics research. Multi-modality and multi-fidelity data assimilation, overcoming poor data quality, parameter identification, super-resolution flow reconstruction and reduced-order modelling are some examples. We hope that this review inspires researchers to develop data-driven models that can address outstanding challenges in the field of cardiovascular biomechanics.

Data accessibility. The codes and data used to generate the results in the paper are available on Github https://github.com/amir-cardiolab/cardio-data-driven.

Authors' contributions. A.A. designed the overall paper and generated the data. A.A. and S.T.M.D. contributed to the mathematical model developments. A.A. and S.T.M.D. both contributed to the writing of the paper.

Competing interests. We declare we have no competing interests.

Funding. A.A. acknowledges funding from NSF OAC grant no. 1947559.

Acknowledgements. The authors would like to thank Milad Habibi for assistance in generating the POD and DMD data in §6 and Dr Roshan M. D'Souza for fruitful discussions related to the topic of the paper. We are also thankful to Dr Steven Brunton and Dr Nathan Kutz for permission to use their codes in several examples in this paper.

References

1. Womersley JR. 1955 Method for the calculation of velocity, rate of flow and viscous drag in arteries when the pressure gradient is known. *J. Physiol.* **127**, 553–563. (doi:10.1113/jphysiol.1955.sp005276)
2. Taylor CA, Fonte TA, Min JK. 2013 Computational fluid dynamics applied to cardiac computed tomography for noninvasive quantification of fractional flow reserve: scientific basis. *J. Am. Coll. Cardiol.* **61**, 2233–2241. (doi:10.1016/j.jacc.2012.11.083)
3. Pearson K. 1901 On lines and planes of closest fit to systems of points in space. *J. Sci.* **2**, 559–572. (doi:10.1080/14786440109462720)
4. Lumley JL. 1967 The structure of inhomogeneous turbulent flows. In *Proc. Int. Colloquium on the Fine Scale Structure of the Atmosphere and its Influence on Radio Wave Propagation* (eds AM Yaglam, VI Tatarsky). Doklady Akademii Nauk SSSR, Moscow, Nauka.
5. Holmes P, Lumley JL, Berkooz G, Rowley CW. 2012 *Turbulence, coherent structures, dynamical systems and symmetry*. Cambridge, UK: Cambridge University Press.
6. Schmid PJ. 2010 Dynamic mode decomposition of numerical and experimental data. *J. Fluid Mech.* **656**, 5–28. (doi:10.1017/S0022112010001217)
7. Brunton SL, Proctor JL, Kutz JN. 2016 Discovering governing equations from data by sparse identification of nonlinear dynamical systems. *Proc. Natl Acad. Sci. USA* **113**, 3932–3937. (doi:10.1073/pnas.1517384113)
8. Candès EJ. 2006 Compressive sampling. In *Proc. Int. Congress of Mathematicians*, vol. 3, pp. 1433–1452. Madrid, Spain: World Scientific.
9. Donoho L. 2006 Compressed sensing. *IEEE Trans. Inf. Theory* **52**, 1289–1306. (doi:10.1109/TIT.2006.871582)
10. Candès EJ, Romberg J, Tao T. 2006 Robust uncertainty principles: exact signal reconstruction from highly incomplete frequency information. *IEEE Trans. Inf. Theory* **52**, 489–509. (doi:10.1109/TIT.2005.862083)
11. Barrault M, Maday Y, Nguyen NC, Patera AT. 2004 An 'empirical interpolation' method: application to efficient reduced-basis discretization of partial differential equations. *C.R. Math.* **339**, 667–672. (doi:10.1016/j.crma.2004.08.006)
12. Chaturantabut S, Sorensen DC. 2010 Nonlinear model reduction via discrete empirical interpolation. *SIAM J. Sci. Comput.* **32**, 2737–2764. (doi:10.1137/090766498)
13. Manohar K, Brunton BW, Kutz JN, Brunton SL. 2018 Data-driven sparse sensor placement for reconstruction: demonstrating the benefits of exploiting known patterns. *IEEE Control Syst. Mag.* **38**, 63–86. (doi:10.1109/MCS.2018.2810460)
14. Brunton SL, Noack BR, Koumoutsakos P. 2020 Machine learning for fluid mechanics. *Annu. Rev. Fluid Mech.* **52**, 477–508. (doi:10.1146/annurev-fluid-010719-060214)
15. Taira K *et al.* 2017 Modal analysis of fluid flows: an overview. *AIAA J.* **55**, 4013–4041. (doi:10.2514/1.J056060)
16. Udell M, Townsend A. 2019 Why are big data matrices approximately low rank? *SIAM J. Math. Data Sci.* **1**, 144–160. (doi:10.1137/18M1183480)
17. Strang G. 2019 *Linear algebra and learning from data*. Wellesley, MA: Wellesley-Cambridge Press.
18. Boyd S, Vandenberghe L. 2018 *Introduction to applied linear algebra: vectors, matrices, and least squares*. Cambridge, UK: Cambridge University Press.
19. Trefethen LN, Bau III D. 1997 *Numerical linear algebra*, vol. 50. Philadelphia, PA: SIAM.
20. Bruce P, Bruce A, Gedeck P. 2020 *Practical statistics for data scientists: 50+ essential concepts using R and Python*. Sebastopol, CA: O'Reilly Media.
21. Meyer MC. 2019 *Probability and mathematical statistics: theory, applications, and practice in R*, vol. 162. Philadelphia, PA: SIAM.
22. Boyd SP, Vandenberghe L. 2004 *Convex optimization*. Cambridge, UK: Cambridge University Press.
23. Perko L. 2013 *Differential equations and dynamical systems*. Berlin, Germany: Springer Science & Business Media.
24. Strogatz SH. 2018 *Nonlinear dynamics and chaos: with applications to physics, biology, chemistry, and engineering*. Boca Raton, FL: CRC Press.

25. Asch M, Bocquet M, Nodet M. 2016 *Data assimilation: methods, algorithms, and applications*. Philadelphia, PA: SIAM.
26. Law K, Stuart A, Zygalakis K. 2015 Data assimilation: a mathematical introduction. Technical report.
27. Majumdar A. 2018 *Compressed sensing for engineers*. Boca Raton, FL: CRC Press.
28. Rish I, Grabarnik G. 2014 *Sparse modeling: theory, algorithms, and applications*. Boca Raton, FL: CRC Press.
29. Burkov A. 2019 *The hundred-page machine learning book*, vol. 1. Quebec, Canada: Andriy Burkov.
30. James G, Witten D, Hastie T, Tibshirani R. 2013 *An introduction to statistical learning*, vol. 112. Berlin, Germany: Springer.
31. Eldén L. 2007 *Matrix methods in data mining and pattern recognition*. Philadelphia, PA: SIAM.
32. Quarteroni A, Manzoni A, Negri F. 2015 *Reduced basis methods for partial differential equations: an introduction*, vol. 92. Berlin, Germany: Springer.
33. Kutz JN, Brunton SL, Brunton BW, Proctor JL. 2016 *Dynamic mode decomposition: data-driven modeling of complex systems*. Philadelphia, PA: SIAM.
34. Kutz JN. 2013 *Data-driven modeling & scientific computation: methods for complex systems & big data*. Oxford, UK: Oxford University Press.
35. Brunton SL, Kutz JN. 2019 *Data-driven science and engineering: machine learning, dynamical systems, and control*. Cambridge, UK: Cambridge University Press.
36. Wold S, Esbensen K, Geladi P. 1987 Principal component analysis. *Chemom. Intell. Lab. Syst.* **2**, 37–52. (doi:10.1016/0169-7439(87)80084-9)
37. Hotelling H. 1933 Analysis of a complex of statistical variables into principal components. *J. Edu. Psychol.* **24**, 417. (doi:10.1037/h0071325)
38. Lumley JL. 2007 *Stochastic tools in turbulence*. New York, NY: Dover Publications.
39. Habibi M, Dawson STM, Arzani A. 2020 Data-driven pulsatile blood flow physics with dynamic mode decomposition. *Fluids* **5**, 111. (doi:10.3390/fluids5030111)
40. Arzani A, Suh GY, Dalman RL, Shadden SC. 2014 A longitudinal comparison of hemodynamics and intraluminal thrombus deposition in abdominal aortic aneurysms. *Am. J. Physiol.-Heart Circ. Physiol.* **307**, H1786–H1795. (doi:10.1152/ajpheart.00461.2014)
41. Arzani A, Shadden SC. 2012 Characterization of the transport topology in patient-specific abdominal aortic aneurysm models. *Phys. Fluids* **24**, 1901. (doi:10.1063/1.4744984)
42. Karmonik C, Partovi S, Loebe M, Schmack B, Weymann A, Lumsden AB, Karck M, Ruhparwar A. 2014 Computational fluid dynamics in patients with continuous-flow left ventricular assist device support show hemodynamic alterations in the ascending aorta. *J. Thorac. Cardiovasc. Surg.* **147**, 1326–1333. (doi:10.1016/j.jtcvs.2013.09.069)
43. Passerini T, Sangalli LM, Vantini S, Piccinelli M, Bacigaluppi S, Antiga L, Boccardi E, Secchi P, Veneziani A. 2012 An integrated statistical investigation of internal carotid arteries of patients affected by cerebral aneurysms. *Cardiovasc. Eng. Technol.* **3**, 26–40. (doi:10.1007/s13239-011-0079-x)
44. Mut F, Wright S, Ascoli GA, Cebral JR. 2014 Morphometric, geographic, and territorial characterization of brain arterial trees. *Int. J. Numer. Methods Biomed. Eng.* **30**, 755–766. (doi:10.1002/cnm.2627)
45. Bruse JL *et al.* 2016 A statistical shape modelling framework to extract 3D shape biomarkers from medical imaging data: assessing arch morphology of repaired coarctation of the aorta. *BMC Med. Imaging* **16**, 40. (doi:10.1186/s12880-016-0142-z)
46. Molony DS, Park J, Zhou L, Fleischer CC, Sun HY, Hu XP, Oshinski JN, Samady H, Giddens DP, Rezvan A. 2019 Bulk flow and near wall hemodynamics of the rabbit aortic arch and descending thoracic aorta: a 4D PC-MRI derived computational fluid dynamics study. *J. Biomech. Eng.* **141**, 0110031–01100311. (doi:10.1115/1.4041222)
47. Cosentino F, Raffa GM, Gentile G, Agnese V, Bellavia D, Pilato M, Pasta S. 2020 Statistical shape analysis of ascending thoracic aortic aneurysm: correlation between shape and biomechanical descriptors. *J. Per. Med.* **10**, 28. (doi:10.3390/jpm10020028)
48. M. Hoeijmakers MJM, Waechter-Stehle I, Weese J, Van de Vosse FN. 2020 Combining statistical shape modeling, CFD, and meta-modeling to approximate the patient-specific pressure-drop across the aortic valve in real-time. *Int. J. Numer. Methods Biomed. Eng.* **36**, e3387.
49. Fonseca CG *et al.* 2011 The cardiac atlas project—an imaging database for computational modeling and statistical atlases of the heart. *Bioinformatics* **27**, 2288–2295. (doi:10.1093/bioinformatics/btr360)
50. Scholkopf B, Smola AJ. 2018 *Learning with kernels: support vector machines, regularization, optimization, and beyond*. Adaptive Computation and Machine Learning series. Cambridge, MA: MIT Press.
51. Ehlert A, Nayeri CN, Morzynski M, Noack BR. 2019 Locally linear embedding for transient cylinder wakes. (http://arxiv.org/abs/1906.07822)
52. Von Luxburg U. 2007 A tutorial on spectral clustering. *Stat. Comput.* **17**, 395–416. (doi:10.1007/s11222-007-9033-z)
53. Agostini L. 2020 Exploration and prediction of fluid dynamical systems using auto-encoder technology. *Phys. Fluids* **32**, 067103. (doi:10.1063/5.0012906)
54. Dauxois J, Pousse A, Romain Y. 1982 Asymptotic theory for the principal component analysis of a vector random function: some applications to statistical inference. *J. Multivariate Anal.* **12**, 136–154. (doi:10.1016/0047-259X(82)90088-4)
55. Valen-Sendstad K, Mardal KA, Mortensen M, Reif BAP, Langtangen HP. 2011 Direct numerical simulation of transitional flow in a patient-specific intracranial aneurysm. *J. Biomech.* **44**, 2826–2832. (doi:10.1016/j.jbiomech.2011.08.015)
56. Candès EJ, Li X, Ma Y, Wright J. 2011 Robust principal component analysis? *J. ACM (JACM)* **58**, 11. (doi:10.1145/1970392.1970395)
57. Scherl I, Strom B, Shang JK, Williams O, Polagye BL, Brunton SL. 2020 Robust principal component analysis for modal decomposition of corrupt fluid flows. *Phys. Rev. Fluids* **5**, 054401. (doi:10.1103/PhysRevFluids.5.054401)
58. Lin Z, Chen M, Ma Y. 2010 The augmented lagrange multiplier method for exact recovery of corrupted low-rank matrices. (http://arxiv.org/abs/1009.5055)
59. Tibshirani R. 1996 Regression shrinkage and selection via the lasso. *J. R. Stat. Soc.: Ser. B* **58**, 267–288.
60. Arzani A. 2018 Accounting for residence-time in blood rheology models: do we really need non-Newtonian blood flow modelling in large arteries? *J. R. Soc. Interface* **15**, 20180486. (doi:10.1098/rsif.2018.0486)
61. Shannon CE. 1948 A mathematical theory of communication. *Bell Syst. Tech. J.* **27**, 379–423. (doi:10.1002/j.1538-7305.1948.tb01338.x)
62. Chen GH, Tang J, Leng S. 2008 Prior image constrained compressed sensing (PICCS): a method to accurately reconstruct dynamic CT images from highly undersampled projection data sets. *Med. Phys.* **35**, 660–663. (doi:10.1118/1.2836423)
63. Jung H, Sung K, Nayak KS, Kim EY, Ye JC. 2009 k-t FOCUSS: a general compressed sensing framework for high resolution dynamic MRI. *Magn. Reson. Med.* **61**, 103–116. (doi:10.1002/mrm.21757)
64. Ma LE *et al.* 2019 Aortic 4D flow MRI in 2 minutes using compressed sensing, respiratory controlled adaptive k-space reordering, and inline reconstruction. *Magn. Reson. Med.* **81**, 3675–3690. (doi:10.1002/mrm.27684)
65. Ibañez R, Abisset-Chavanne E, Cueto E, Ammar A, Duval JL, Chinesta F. 2019 Some applications of compressed sensing in computational mechanics: model order reduction, manifold learning, data-driven applications and nonlinear dimensionality reduction. *Comput. Mech.* **64**, 1259–1271. (doi:10.1007/s00466-019-01703-5)
66. Candès EJ, Wakin MB. 2008 An introduction to compressive sampling. *IEEE Signal Process Mag.* **25**, 21–30. (doi:10.1109/MSP.2007.914731)
67. Evensen G. 2009 *Data assimilation: the ensemble Kalman filter*. Berlin, Germany: Springer Science & Business Media.
68. Falahatpisheh A, Pedrizzetti G, Kheradvar A. 2014 Three-dimensional reconstruction of cardiac flows based on multi-planar velocity fields. *Exp. Fluids* **55**, 1848. (doi:10.1007/s00348-014-1848-8)
69. Falahatpisheh A, Kheradvar A. 2015 A measure of axisymmetry for vortex rings. *Eur. J. Mech.-B/Fluids* **49**, 264–271. (doi:10.1016/j.euromechflu.2014.09.003)
70. Gaidzik F, Stucht D, Roloff C, Speck O, Thévenin D, Janiga G. 2019 Transient flow prediction in an idealized aneurysm geometry using data assimilation. *Comput. Biol. Med.* **115**, 103507. (doi:10.1016/j.compbiomed.2019.103507)
71. DeVault K, Gremaud PA, Novak V, Olufsen MS, Vernieres G, Zhao P. 2008 Blood flow in the circle of Willis: modeling and calibration. *Multiscale Model. Simul.* **7**, 888–909. (doi:10.1137/07070231X)
72. Canuto D, Pantoja JL, Han J, Dutson EP, Eldredge JD. 2020 An ensemble Kalman filter approach to

parameter estimation for patient-specific cardiovascular flow modeling. *Theor. Comput. Fluid Dyn.* **34**, 1–24. (doi:10.1007/s00162-020-00530-2)

73. Pant S, Fabrèges B, Gerbeau JF, Vignon-Clementel IE. 2014 A methodological paradigm for patient-specific multi-scale CFD simulations: from clinical measurements to parameter estimates for individual analysis. *Int. J. Numer. Methods Biomed. Eng.* **30**, 1614–1648. (doi:10.1002/cnm.2692)
74. Arnold A, Battista C, Bia D, German YZ, Armentano RL, Tran H, Olufsen MS. 2017 Uncertainty quantification in a patient-specific one-dimensional arterial network model: EnKF-based inflow estimator. *J. Verif. Validation Uncertainty Quantif.* **2**, 011002. (doi:10.1115/1.4035918)
75. Bertoglio C, Moireau P, Gerbeau JF. 2012 Sequential parameter estimation for fluid–structure problems: application to hemodynamics. *Int. J. Numer. Methods Biomed. Eng.* **28**, 434–455. (doi:10.1002/cnm.1476)
76. Funke SW, Nordaas M, Evju Ø, Alnæs MS, Mardal KA. 2019 Variational data assimilation for transient blood flow simulations: cerebral aneurysms as an illustrative example. *Int. J. Numer. Methods Biomed. Eng.* **35**, e3152. (doi:10.1002/cnm.3152)
77. Rispoli VC, Nielsen JF, Nayak KS, Carvalho JLA. 2015 Computational fluid dynamics simulations of blood flow regularized by 3D phase contrast MRI. *Biomed. Eng. Online* **14**, 110. (doi:10.1186/s12938-015-0104-7)
78. Fathi MF, Bakhshinejad A, Baghaie A, Saloner D, Sacho RH, Rayz VL, D'Souza RM. 2018 Denoising and spatial resolution enhancement of 4D flow MRI using proper orthogonal decomposition and lasso regularization. *Comput. Med. Imaging Graph* **70**, 165–172. (doi:10.1016/j.compmedimag.2018.07.003)
79. Koltukluoğlu TS, Blanco PJ. 2018 Boundary control in computational haemodynamics. *J. Fluid Mech.* **847**, 329–364. (doi:10.1017/jfm.2018.329)
80. Annio G, Torii R, Ariff B, O'Regan DP, Muthurangu V, Ducci A, Tsang V, Burriesci G. 2019 Enhancing magnetic resonance imaging with computational fluid dynamics. *J. Eng. Sci. Med. Diagn. Therapy* **2**, 041010. (doi:10.1115/1.4045493)
81. Ferdian E, Suinesiaputra A, Dubowitz DJ, Zhao D, Wang A, Cowan B, Young AA. 2020 4DFlowNet: super-resolution 4D flow MRI using deep learning and computational fluid dynamics. *Front. Phys.* **8**, 138. (doi:10.3389/fphy.2020.00138)
82. Berkooz G, Holmes P, Lumley JL. 1993 The proper orthogonal decomposition in the analysis of turbulent flows. *Annu. Rev. Fluid Mech.* **25**, 539–575. (doi:10.1146/annurev.fl.25.010193.002543)
83. Noack BR. 2016 From snapshots to modal expansions—bridging low residuals and pure frequencies. *J. Fluid Mech.* **802**, 1–4. (doi:10.1017/jfm.2016.416)
84. Rowley CW, Mezić I, Bagheri S, Schlatter P, Henningson DS. 2009 Spectral analysis of nonlinear flows. *J. Fluid Mech.* **641**, 115–127. (doi:10.1017/S0022112009992059)
85. Tu JH, Rowley Clarence W, Luchtenburg DM, Brunton SL, Kutz JN. 2014 On dynamic mode decomposition: theory and applications. *J. Comput. Dyn.* **1**, 391–421. (doi:10.3934/jcd.2014.1.391)
86. Sirovich L. 1987 Turbulence and the dynamics of coherent structures, parts I–III. *Q. Appl. Math.* **XLV**, 561–590. (doi:10.1090/qam/910462)
87. Epps BP, Techet AH. 2010 An error threshold criterion for singular value decomposition modes extracted from PIV data. *Exp. Fluids* **48**, 355–367. (doi:10.1007/s00348-009-0740-4)
88. Wynn A, Pearson D, Ganapathisubramani B, Goulart P. 2013 Optimal mode decomposition for unsteady flows. *J. Fluid Mech.* **733**, 473–503. (doi:10.1017/jfm.2013.426)
89. Sashittal P, Bodony DJ. 2019 Reduced-order control using low-rank dynamic mode decomposition. *Theor. Comput. Fluid Dyn.* **33**, 603–623. (doi:10.1007/s00162-019-00508-9)
90. Jovanović MR, Schmid PJ, Nichols JW. 2014 Sparsity-promoting dynamic mode decomposition. *Phys. Fluids* **26**, 024103. (doi:10.1063/1.4863670)
91. Drmac Z, Mezic I, Mohr R. 2018 Data driven modal decompositions: analysis and enhancements. *SIAM J. Sci. Comput.* **40**, A2253–A2285. (doi:10.1137/17M1144155)
92. Zhang H, Dawson STM, Rowley CW, Deem EA, Cattafesta LN. 2020 Evaluating the accuracy of the dynamic mode decomposition. *J. Comput. Dyn.* **7**, 35. (doi:10.3934/jcd.2020002)
93. Rowley CW, Dawson STM. 2017 Model reduction for flow analysis and control. *Annu. Rev. Fluid Mech.* **49**, 387–417. (doi:10.1146/annurev-fluid-010816-060042)
94. Proctor J, Brunton S, Kutz J. 2016 Dynamic mode decomposition with control. *SIAM J. Appl. Dyn. Syst.* **15**, 142–161. (doi:10.1137/15M1013857)
95. Williams M, Kevrekidis I, Rowley C. 2015 A data-driven approximation of the Koopman operator: extending dynamic mode decomposition. *J. Nonlinear Sci.* **25**, 1307–1346. (doi:10.1007/s00332-015-9258-5)
96. Dawson STM, Hemati MS, Williams MO, Rowley CW. 2016 Characterizing and correcting for the effect of sensor noise in the dynamic mode decomposition. *Exp. Fluids* **57**, 42. (doi:10.1007/s00348-016-2127-7)
97. Hemati MS, Rowley CW, Deem EA, Cattafesta LN. 2017 De-biasing the dynamic mode decomposition for applied Koopman spectral analysis of noisy datasets. *Theor. Comput. Fluid Dyn.* **31**, 349–368. (doi:10.1007/s00162-017-0432-2)
98. Askham T, Kutz JN. 2018 Variable projection methods for an optimized dynamic mode decomposition. *SIAM J. Appl. Dyn. Syst.* **17**, 380–416. (doi:10.1137/M1124176)
99. Logg A, Mardal KA, Wells G. 2012 *Automated solution of differential equations by the finite element method*, vol. 84. Berlin, Germany: Springer.
100. Grinberg L, Yakhot A, Karniadakis G. 2009 Analyzing transient turbulence in a stenosed carotid artery by proper orthogonal decomposition. *Ann. Biomed. Eng.* **37**, 2200–2217. (doi:10.1007/s10439-009-9769-z)
101. Kefayati S, Poepping TL. 2013 Transitional flow analysis in the carotid artery bifurcation by proper orthogonal decomposition and particle image velocimetry. *Med. Eng. Phys.* **35**, 898–909. (doi:10.1016/j.medengphy.2012.08.020)
102. Di Labbio G, Kadem L. 2019 Reduced-order modeling of left ventricular flow subject to aortic valve regurgitation. *Phys. Fluids* **31**, 031901. (doi:10.1063/1.5083054)
103. Bright I, Lin G, Kutz JN. 2013 Compressive sensing based machine learning strategy for characterizing the flow around a cylinder with limited pressure measurements. *Phys. Fluids* **25**, 127102. (doi:10.1063/1.4836815)
104. Drmac Z, Gugercin S. 2016 A new selection operator for the discrete empirical interpolation method—improved a priori error bound and extensions. *SIAM J. Sci. Comput.* **38**, A631–A648. (doi:10.1137/15M1019271)
105. Cho YI, Mooney MP, Cho DJ. 2008 Hemorheological disorders in diabetes mellitus. *J. Diabetes Sci. Technol.* **2**, 1130–1138. (doi:10.1177/193229680800200622)
106. Hughes TJR, Cottrell JA, Bazilevs Y. 2005 Isogeometric analysis: CAD, finite elements, NURBS, exact geometry and mesh refinement. *Comput. Methods Appl. Mech. Eng.* **194**, 4135–4195. (doi:10.1016/j.cma.2004.10.008)
107. Hesthaven JS, Rozza G, Stamm B. 2016 *Certified reduced basis methods for parametrized partial differential equations*, vol. 590. Berlin, Germany: Springer.
108. Zare A, Georgiou TT, Jovanović MR. 2020 Stochastic dynamical modeling of turbulent flows. *Annu. Rev. Control Rob. Auton. Syst.* **3**, 195–219. (doi:10.1146/annurev-control-053018-023843)
109. Hansen KB, Shadden SC. 2019 Automated reduction of blood coagulation models. *Int. J. Numer. Methods Biomed. Eng.* **35**, e3220. (doi:10.1002/cnm.3220)
110. Papadopoulos KP, Gavaises M, Atkin C. 2014 A simplified mathematical model for thrombin generation. *Med. Eng. Phys.* **36**, 196–204. (doi:10.1016/j.medengphy.2013.10.012)
111. Papadopoulos K. 2015 Flow effect on thrombus formation in stenosed coronary arteries: a computational study. PhD thesis, City, University of London.
112. Brunton SL, Proctor JL, Kutz JN. 2016 Sparse identification of nonlinear dynamics with control (SINDYc). *IFAC-PapersOnLine* **49**, 710–715. (doi:10.1016/j.ifacol.2016.10.249)
113. Arzani A, Masters KS, Mofrad MRK. 2017 Multiscale systems biology model of calcific aortic valve disease progression. *ACS Biomater. Sci. Eng.* **3**, 2922–2933. (doi:10.1021/acsbiomaterials.7b00174)
114. Sree VD, Tepole AB. 2020 Computational systems mechanobiology of growth and remodeling: integration of tissue mechanics and cell regulatory network dynamics. *Curr. Opin. Biomed. Eng.* **15**, 75–80. (doi:10.1016/j.cobme.2020.01.002)
115. Cortiella A, Park KC, Doostan A. 2020 Sparse identification of nonlinear dynamical systems via

reweighted ℓ_1-regularized least squares. (http://arxiv.org/abs/2005.13232)

116. Rudy SH, Brunton SL, Proctor JL, Kutz JN. 2017 Data-driven discovery of partial differential equations. *Sci. Adv.* **3**, e1602614. (doi:10.1126/sciadv.1602614)
117. Detmer FJ, Lückehe D, Mut F, Slawski M, Hirsch S, Bijlenga P, von Voigt G, Cebral JR. 2020 Comparison of statistical learning approaches for cerebral aneurysm rupture assessment. *Int. J. Comput. Assist. Radiol. Surg.* **15**, 141–150. (doi:10.1007/s11548-019-02065-2)
118. Jiang Z, Do HN, Choi J, Lee W, Baek S. 2020 A deep learning approach to predict abdominal aortic aneurysm expansion using longitudinal data. *Front. Phys.* **7**, 235. (doi:10.3389/fphy.2019.00235)
119. Duraisamy K, Iaccarino G, Xiao H. 2019 Turbulence modeling in the age of data. *Annu. Rev. Fluid Mech.* **51**, 357–377. (doi:10.1146/annurev-fluid-010518-040547)
120. Antiga L, Steinman DA. 2009 Rethinking turbulence in blood. *Biorheology* **46**, 77–81. (doi:10.3233/BIR-2009-0538)
121. Xu D, Varshney A, Ma X, Song B, Riedl M, Avila M, Hof B. 2020 Nonlinear hydrodynamic instability and turbulence in pulsatile flow. *Proc. Natl Acad. Sci. USA* **117**, 11 233–11 239. (doi:10.1073/pnas.1913716117)
122. Coenen A *et al.* 2018 Diagnostic accuracy of a machine-learning approach to coronary computed tomographic angiography-based fractional flow reserve: result from the MACHINE consortium. *Circulation: Cardiovasc. Imag.* **11**, e007217.
123. Sarrami-Foroushani A, Lassila T, Pozo JM, Gooya A, Frangi AF. 2016 Direct estimation of wall shear stress from aneurysmal morphology: a statistical approach. In *Int. Conf. on Medical Image Computing and Computer-Assisted Intervention, Athens, Greece, 17–21 October 2016*, pp. 201–209. Berlin, Germany: Springer.
124. Succi S, Coveney PV. 2019 Big data: the end of the scientific method? *Phil. Trans. R. Soc. A* **377**, 20180145. (doi:10.1098/rsta.2018.0145)
125. Raissi M, Perdikaris P, Karniadakis GE. 2019 Physics-informed neural networks: a deep learning framework for solving forward and inverse problems involving nonlinear partial differential equations. *J. Comput. Phys.* **378**, 686–707. (doi:10.1016/j.jcp.2018.10.045)
126. Raissi M, Yazdani A, Karniadakis GE. 2020 Hidden fluid mechanics: learning velocity and pressure fields from flow visualizations. *Science* **367**, 1026–1030. (doi:10.1126/science.aaw4741)
127. Fathi MF, Perez-Raya I, Baghaie A, Berg P, Janiga G, Arzani A, D'Souza RM. 2020 Super-resolution and denoising of 4D-flow MRI using physics-informed deep neural nets. *Comput. Methods Programs Biomed.* **197**, 105729. (doi:10.1016/j.cmpb.2020.105729)
128. Benner P, Gugercin S, Willcox K. 2015 A survey of projection-based model reduction methods for parametric dynamical systems. *SIAM Rev.* **57**, 483–531. (doi:10.1137/130932715)
129. Peng GCY *et al.* In press. Multiscale modeling meets machine learning: what can we learn? *Arch. Comput. Methods Eng.* (doi:10.1007/s11831-020-09405-5)
130. Perdikaris P, Raissi M, Damianou A, Lawrence ND, Karniadakis GE. 2016 Nonlinear information fusion algorithms for robust multi-fidelity modeling. *Proc. R. Soc. A* **473**, 20160751. (doi:10.1098/rspa.2016.0751)
131. Cai S, Wang Z, Lu L, Zaki TA, Karniadakis GE. 2020 DeepM&Mnet: inferring the electroconvection multiphysics fields based on operator approximation by neural networks. (http://arxiv.org/abs/2009.12935)
132. von Rueden L, Mayer S, Sifa R, Bauckhage C, Garcke J. 2020 Combining machine learning and simulation to a hybrid modelling approach: current and future directions. In *Int. Symp. on Intelligent Data Analysis, Konstanz, Germany, 27–29 April 2020*, pp. 548–560. Berlin, Germany: Springer.
133. Kapteyn MG, Willcox KE. 2020 From physics-based models to predictive digital twins via interpretable machine learning. (http://arxiv.org/abs/2004.11356)
134. Hose DR, Lawford PV, Huberts W, Hellevik LR, Omholt SW, van de Vosse FN. 2019 Cardiovascular models for personalised medicine: where now and where next? *Med. Eng. Phys.* **72**, 38–48. (doi:10.1016/j.medengphy.2019.08.007)